University of Bremen

Master Thesis

Atmospheric Correction of Brightness Temperatures for Sea Ice Concentration Retrieval using 89 GHz Algorithms

Author:

Junshen Lu

Supervisor:

Dr. Georg Heygster

A thesis submitted in fulfilment of the requirements

for the degree of Master of Science

in the

PHAROS

IUP

November 2014

Declaration of Authorship

I, Junshen Lu, declare that this thesis titled, 'Atmospheric Correction of Brightness Temperatures for Sea Ice Concentration Retrieval using 89 GHz Algorithms' and the work presented in it are my own. I confirm that:

- This work was done wholly or mainly while in candidature for a research degree at this University.
- Where any part of this thesis has previously been submitted for a degree or any other qualification at this University or any other institution, this has been clearly stated.
- Where I have consulted the published work of others, this is always clearly attributed.
- Where I have quoted from the work of others, the source is always given. With the exception of such quotations, this thesis is entirely my own work.
- I have acknowledged all main sources of help.
- Where the thesis is based on work done by myself jointly with others, I have made clear exactly what was done by others and what I have contributed myself.

Signed: ____

Date: ____

UNIVERSITY OF BREMEN

Abstract

Master of Science

Atmospheric Correction of Brightness Temperatures for Sea Ice Concentration Retrieval using 89 GHz Algorithms

by Junshen Lu

Sea ice has large impact on climate changes. An accurate retrieval of the spatial and temporal distribution of sea ice is thus essential to understand and predict the weather and climate. Taking advantage of the high resolution of AMSR-E (Advanced Microwave Scanning Radiometer - Earth Observing System) 89 GHz channel, the *ASI* (Artist Sea Ice) algorithm has a higher spatial resolution, but is more sensitive to the atmospheric impact. In this study, the influence of atmospheric parameters on sea ice concentration retrieval in the Arctic is studied, and a new version of *ASI* algorithm that includes atmospheric correction is developed. The correction is carried out by simulating TB contributed by atmosphere with a linear forward model developed for the frequencies of AMSR-E. ECMWF data, co-located with AMSR-E measurements, are used as the atmosphere profiles. The included parameters are: total columnar water vapor, wind speed, liquid water path, skin temperature and 2 meter air temperature. The combined correction of TWV, WS, LWP and T_{skin} effectively screens out most atmospheric influences.

Acknowledgements

First of all I would like to express my deep gratitude to Prof.Dr.Justus Notholt, and Dr.Georg Heygster for their supervision, guidance and support during the planning and development of this research work. I would like to say thank you to Dr.Leif Toudal Pederson from Danish Meteorological Institute for providing me with the validation data and radiative transfer model, and for his valuable suggestions in evaluating atmospheric correction. I would also like to thank Dr.Christian Melsheimer, for his help and advice in IDL programming. My grateful thanks are also extended to all the co-workers in the *PHAROS* group for the amazing working environment and their enthusiastic encouragement. I would also like to extend my thanks to the fellow students in the PEP program for the two years of wonderful life here in Bremen. Finally, I wish to thank my parents and friends for their support and encouragement throughout my study.

Contents

List of Figures

List of Tables

Dedicated to my family and friends

Chapter 1

Introduction

1.1 The Role of Sea Ice in the Climate System

Sea ice, as a major component of cryosphere, has a significant impact on the heat transfer and salt fluxes in polar regions and hence drives global climate changes. 5% - 8% of the ocean is covered by sea ice (Comiso et al., 2003). Because of its high albedo, sea ice effectively reduces the absorption of solar radiation, and thus contributes to a positive feedback mechanism for climate cooling: an initial drop of temperature would cause increasing sea ice formation, which leads to less absorption of solar radiation and results in further cooling. Due to its lower density ice floats on the sea surface, and diminishes the heat transfer between ocean and atmosphere because of the low heat conduction. The formation of sea ice at high latitude belongs to the key mechanism that initializes deep water circulation. As the crystallization of ice proceeds, most of its salt content is ejected out into the ocean, which increases the salinity and density of the surrounding water and causes it to sink. The melting of sea ice has the opposite effect. It prevents the deep water up-welling and reduces the oxygen content of ocean water by creating a layer of water of low salinity on the ocean surface. Due to its important role in numerous climate mechanisms, an accurate retrieval of the spatial and temporal distribution of sea ice is essential to understand and predict the weather and climate, while the hostile polar environment restricts the amount of direct measurements and results in insufficient data. Our solution to such dilemma is to use satellite passive microwave remote sensing to get the complete daily image of Arctic and Antarctic sea ice.

1.2 Advantages of Passive Microwave Remote Sensing

Passive microwave remote sensing measures the thermal radiation emitted by the target itself, or the radiation of some natural source scattered by the target in the microwave spectrum (3 GHz to 300 GHz), such as down-welling sky emission, which allows us to continuously observe the states of the Earth regardless of the illumination conditions. It has a wide range of applications from measuring the water vapour content in the atmosphere to monitoring Earth surface information such as sea ice concentration. Granted by the long wavelength of microwave spectrum, atmospheric scattering, the main source of noise, is negligible at most frequencies. This provides an advantage since the strength of atmospheric scattering increases rapidly with the particle size while particle size distribution is difficult to measure. When monitoring the Earth surface, the emitted thermal radiation is first absorbed or scattered by the atmosphere before reaching the satellite antenna, which introduces atmospheric noise. At microwave frequencies below 10 GHz, the atmosphere is transparent, even with the occurrence of clouds, rain or snowfall. At higher microwave frequencies, the atmospheric influences are no longer negligible, hence various weather filters have been developed. For these reasons, passive microwave sensors have been applied for extensive studies of the cryosphere including the retrieval of sea ice concentration, snow cover and ice temperatures for over four decades since the start of the ESMR (Electrically Scanning Microwave Radiometer) sensor in December 1972 (Spreen et al., 2008). At higher microwave frequencies, the atmospheric influences are no longer negligible. Therefore various weather filters have been developed.

1.3 Overview of Microwave Radiometers

Since its launch in 2002 on the AQUA platform, AMSR-E (Advanced Microwave Scanning Radiometer – Earth Observing System) has been widely used for global sea ice observation, until its reflecting dish stopped spinning in October, 2012. Designed and provided by the Japan Aerospace Exploration Agency (JAXA), AMSR-E measures in both polarizations (h-pol and v-pol) at six frequency channels ranging from 6.9 to 89 GHz at the incident angle of 55° with an increasing spatial resolution. Table 1.1 shows the instrument characteristics of AMSR-E.

TABLE 1.1: AMSR-E Instrument Characteristics (Imaoka et al., 2002)

Center Freq. (GHz)	Band Width (MHz)	3dB Beam Width AMSR/AMSR-E (deg)	Ground IFOV Scan x along track AMSR/AMSR-E (km)	NEΔT @150K (K)
6.925	350	1.8 / 2.2	40x70 / 43x75	0.34
10.65	100	1.2 / 1.5	27x46 / 29x51	0.7
18.7	200	0.65 / 0.8	14x25 / 16x27	0.7
23.8	400	0.75 / 0.92	17x29 / 18x32	0.6
36.5	1000	0.35 / 0.42	8x14 / 8x14	0.7
50.3	200	0.25 / -	6x10 / -	1.8
52.8	400	0.25 / -	6x10 / -	1.6
89.0A	3000	0.15 / 0.19	3x6 / 4x7	1.2
89.0B	3000	0.15 / 0.19	3x6 / 4x6	1.2

Antenna	Offset parabolic antenna; effective aperture size 2.0 m for AMSR, 1.6 m for AMSR-E
Polarization	Vertical and Horizontal (only Vertical for 50-GHz band)
Sampling interval, Scan x along track	AMSR: 10x10km (5x5 km for 89GHz) AMSR-E: 9x10km (4.5x4 km for 89GHz A→B, 4.5x6 km for 89GHz B→A)
Incidence angle	55 degrees (54.5 degrees for 89B)
Dynamic range	2.7 - 340 K
Swath width	AMSR: 1600 km, AMSR-E: 1450 km
Integration time	2.5 msec (1.2 msec for 89GHz)
Quantization	10 bit (12 bit for 6.925 GHz)
Scan rate	40 rpm (1.5sec per scan)

Compared to SSM/I (the Special Sensor Microwave Imager) 85 GHz channels, AMSR-E has improved the spatial resolution by a factor of three for the 89 GHz

Table 1.2: Comparetive Operating Characteristics of SSM/I and AMSR (ams, 2014).

AMSR-E		SSM/I	
Frequency (GHz)	IFOV (km²)	Frequency (GHz)	IFOV (km²)
18.7	27 × 16	19.4	69 × 43
23.8	32 × 18	22.2	60 × 40
36.5	14 × 8	37	37 × 28
89	6 × 4	85.5	15 × 13

channels (SSM/I 85 GHz footprint size 15 × 13 km^2, AMSR-E 89 GHz footprint size: 6 × 4 km^2) (Imaoka et al., 2002), as shown in Table 1.2.

1.4 Sea Ice Concentration Retrieval In Arctic

Due to our inability to make constant direct measurements in polar regions, measurements of passive microwave imager are used to retrieve sea ice concentrations. A number of retrieval algorithms have been developed to establish the relationship between the direct measurement results – brightness temperatures and sea ice concentration, based on the different spectral characteristic of water and ice in the microwave spectrum. The retrieval algorithm used in this study is the ARTIST sea ice concentration retrieval algorithm (ASI algorithm), which was originally developed to benefit from the high spatial resolution of SSM/I at 85 GHz, and then adapted to AMSR-E measurements at 89 GHz (Spreen et al., 2008). The ASI algorithm distinguishes water from ice by the polarization difference (P) at 89 GHz, which is similar for first-year ice and multi-year ice, and is much higher for open water (see Figure 1.1).

Compared to other frequently used algorithms such as NASA Team, Bootstrap, etc., theASI algorithm uses a much higher frequency, which has finer spatial resolution but also larger atmospheric influence.

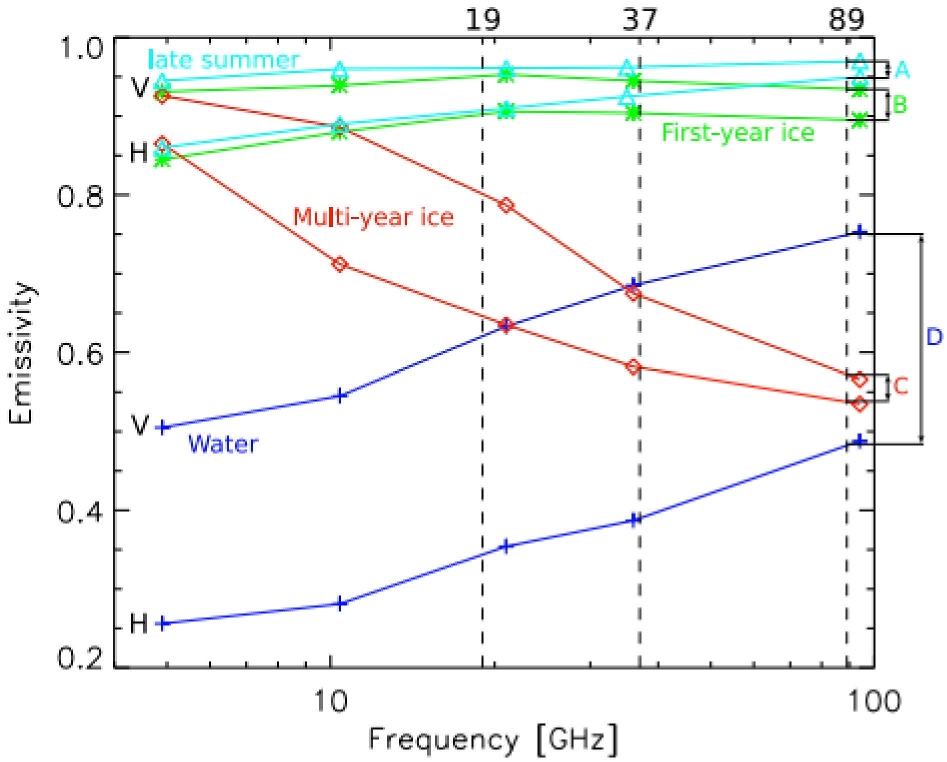

FIGURE 1.1: The spectral variation of emissivities of late summer ice, first-year ice, multi-year ice and water at both polarizations at AMSR-E frequencies. At 89 GHz, the polarization difference for first-year ice (A & B) and multi-year ice (C) are both low, whereas that for water (D) is significantly high. (Spreen et al., 2008)

1.5 Importance of Atmospheric Correction

As the passive microwave imager orbits around the Earth and observes the Earth's surface, the signal it receives is a combination of the scattered down-welling atmospheric emission (T_{BD}), the up-welling atmospheric emission (T_{BU}) and the surface thermal radiation ($T_{B,surface}$), all of which are attenuated by the atmosphere. At higher microwave frequencies, the effect of such atmospheric attenuation, especially that caused by total columnar water vapour and by high cloud liquid water content, is more pronounced. Certain weather filters based on the gradient ratio of brightness temperatures at lower frequencies have been developed to screen out the high water vapour and cloud liquid water case over open water, whereas a more detailed atmospheric correction including all major geophysical states: water vapour, wind speed, surface temperature and liquid water path, for both open water and ice has not yet been accomplished. The aim of this study is to asses the influence of each atmospheric parameter on the satellite measured brightness temperatures in both polarizations at 89 GHz, correct the impact of the atmosphere on the brightness temperatures, and develop an improved *ASI* algorithm which includes atmospheric correction.

Chapter 2

Methodology

2.1 Data Sets

AMSR-E measures at two polarizations and at six different frequency channels ranging from 6.9 to 89 GHz at the incident angle 55°. Both 89 GHz channels are used by the ASI algorithm to retrieve the ice concentration. Granted by the high spatial resolution of 89 GHz channels, ASI sea ice concentration improves the horizontal resolution by a factor of four compared to the widely used Bootstrap algorithm, and thus reveals more fine structures of ice, such as leads and near the ice edge (Beitsch et al., 2014). However, 89 GHz channels have higher sensitivity to the atmosphere as well, which eventually influences the retrieved ice concentration. This work studies the influence of various atmospheric parameters on the brightness temperatures measured in both polarizations at 89 GHz by AMSR-E, develops an atmospheric correction procedure for ASI algorithm, and evaluates the atmospheric impact on the ice concentrations retrieved using the ASI algorithm.

A reference dataset of brightness temperatures and validated ice concentrations taken from the Round Robin Data Package (RRDP), produced in the context of the European Space Agency Sea Ice Climate Change Initiative project (ESA SICCI), is used in this study to evaluate the atmospheric influence on AMSR-E 89 GHz brightness temperatures and ASI ice concentrations. It consists of more than 4000 AMSR-E Level 2 spatially re-sampled brightness temperatures at all frequencies located in the Arctic from all months in 2008, among which 3254 data points are over validated open water, and the remaining 1052 data points are over validated 100% ice concentrations. Figure 2.1 shows the locations of data points with 0% ice concentration. Green data points are measured in summer. Blue are winter data points, and red are points measured in all months. The location of 100% ice concentration sites are shown in Figure 2.2. The horizontal resolution of the reference dataset is 25 km, similar to the resolution of AMSR-E 18 GHz channel, i.e. 21 km.

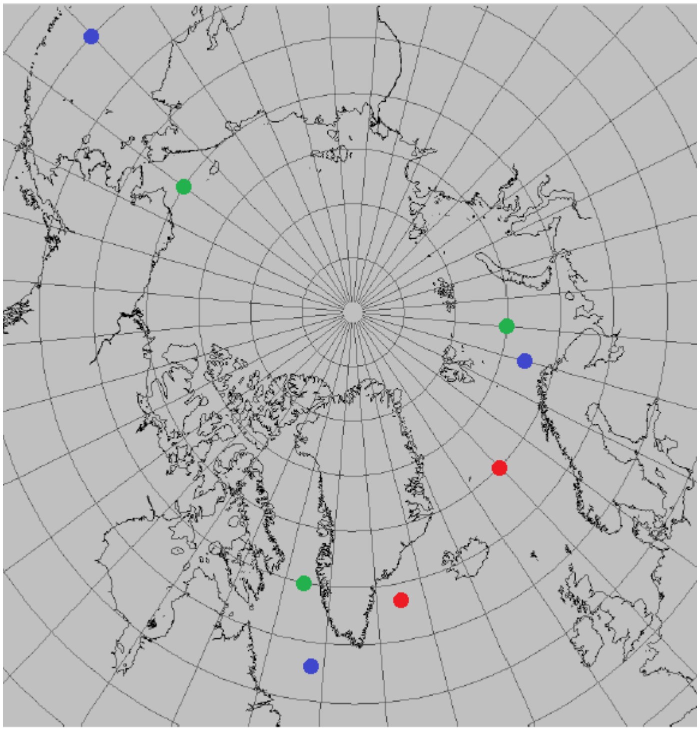

FIGURE 2.1: The location of 0% ice concentration validation sites. Data points in green dots are measured in summer. Blue are winter data points, and red are points measured in all months (Pedersen and Saldo, 2012).

The validation procedure of the reference ice concentration adopts the data of various satellites. The ice drift dataset from ENVISAT (Environmental Satellite) ASAR (Advanced Synthetic Aperture Radar) in areas of high ice concentration are used to determine the regions of 100% ice concentrations. It is assumed that in near 100% ice area, after one day's convergence, the small water fraction of the area is either frozen up or closed by ridging. However, this assumption is

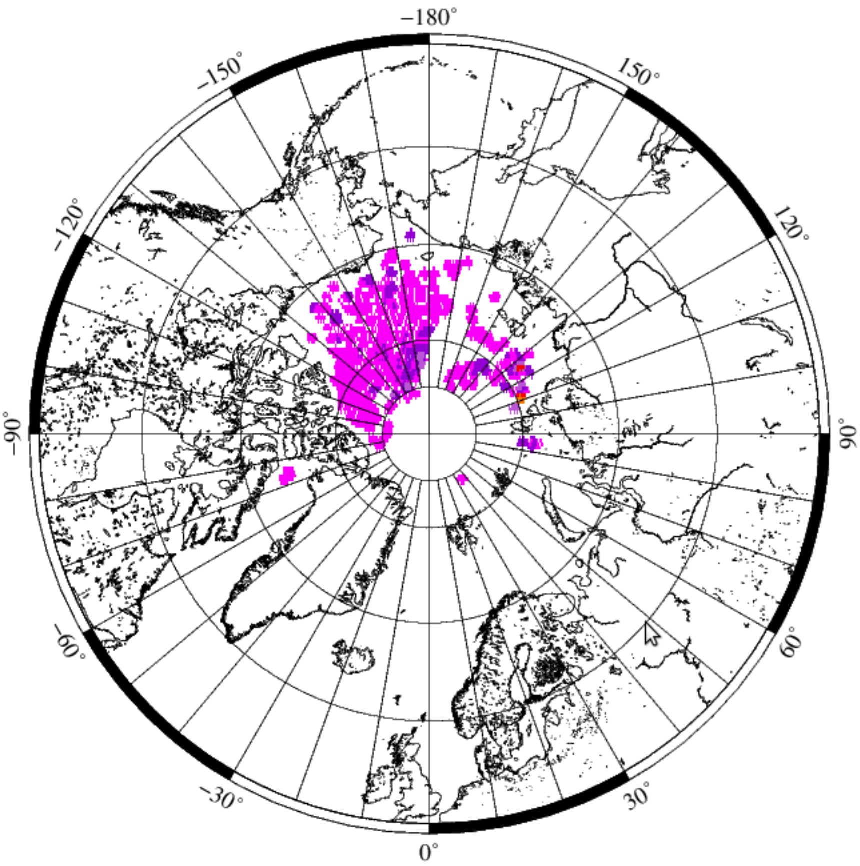

Figure 2.2: The location of 100% ice concentration validation sites.

less reliable in summer due to the existence of melt ponds. Near 100% thin ice is detected by high quality SMOS (Soil Moisture and Ocean Salinity) datasets of large areas (areas in the order of 100 km × 100 km)(Heygster et al., 2014). Open water areas at high latitude are identified from ice charts, climatology and classified satellite images (Pedersen and Saldo, 2012).

The atmospheric states of the satellite measurements are described by the collocated European Centre for Medium Range Weather Forecast (ECMWF) global atmospheric reanalysis product ERA-Interim. ERA-Interim was initially produced to prepare an extended reanalysis to replace ERA-40, one of the three major ECMWF reanalyses used for describing the states of atmosphere, land and ocean-wave conditions from mid-1957 to mid-2002. It is the latest reanalyses to profile atmosphere states, which provides daily analysis from 1979 until present (ECMWF, 2008). Compared to ERA-40, ERA-Interim has more pressure levels (from 23 to 37), and includes more products. The detailed product list of ERA-Interim is described in (Berrisford et al., 2011). Reduced Gaussian grid of the resolution N128 (128 latitude circles, pole to equator) is used in the model. The final atmospheric products have the resolution of 1.5° longitude × 1.5° latitude. The temporal resolution of ERA-Interim is 6 hours (Dee et al., 2011). Here we use part of the parameters from ERA-Interim products, i.e. total columnar water vapour (TWV), wind speed at ten meter height (WS), air temperature at two meter height (T_{2m}), skin temperature (T_{sk}), liquid water path (LWP) and ice water path (IWP), which are required in the forward model to simulate brightness temperatures.

Note that the spatial and temporal resolution of the required satellite measurements (89 GHz) are much higher than that of the modelled atmosphere profiles. This difference has an impact on the accuracy of simulated brightness temperatures, and will be discussed in detail in Chapter 3.2.1 and 3.2.2.

2.2 Radiative Transfer Models Used For Atmospheric Correction

As the radiometer orbits around the Earth and observes the Earth's surface, the signal it receives is a combination of the scattered down-welling atmospheric emission (T_{BD}), the up-welling atmospheric emission (T_{BU}) and the surface thermal radiation ($T_{B,surface}$), all of which are attenuated by the atmosphere. The relationship between the brightness temperature (T_B) measured by the radiometer and the geophysical states is described by the radiative transfer model (RTM). In addition to the well collocated geophysical profiles, an accurate RTM is crucial for simulating brightness temperatures of the target. In this study, AMSR Ocean Algorithm (Wentz and Meissner, 2000) is used as the RTM to simulate brightness temperatures. Henceforth, it will be referred as the Wentz forward model. The Wentz forward model is a linearised radiative transfer model at AMSR-E frequencies and incidence angle. It consists of three main components. The core is a radiative transfer equation that determines how much of the surface thermal emission and scattered down-welling sky radiation is transferred to the satellite antenna. the other two components are the atmosphere model and the sea-surface model.

We begin by deriving the 1-d radiative transfer equation for the atmosphere bounded at the surface of Earth and the top of cold space. In the microwave spectrum, the thermal radiation is usually expressed in the term of brightness temperature. At position s in the atmosphere, the change of brightness temperature is due to the absorption of radiation arriving at s and to microwave emission from position s. The governing differential equation of the radiative transfer is :

$$\frac{\partial T_B}{\partial s} = -\alpha(s)[T_B(s) - T(s)] \tag{2.1}$$

where s is the distance along some path in the atmosphere, $\alpha(s)$ is the absorption coefficient, and *T(s)* is the physical temperature of the atmosphere at position s.

By integrating both sides of this equation from $s = 0$ (the Earth's surface) to $s = S$ (the top of atmosphere), we get the up-welling and down-welling atmospheric emissions:

$$T_{BU} = \int_0^S \mathrm{d}s\, \alpha(s) T(s) \exp\left(-\int_s^S \mathrm{d}s\, \alpha(s)\right) \tag{2.2}$$

$$T_{BD} = \int_0^S \mathrm{d}s\, \alpha(s) T(s) \exp\left(-\int_0^s \mathrm{d}s\, \alpha(s)\right) \tag{2.3}$$

To simplify the expression, we define the atmospheric terms by the transmittance function τ between position s_1 and s_2:

$$\tau(s_1, s_2) = \exp\left(-\int_{s_1}^{s_2} \mathrm{d}s\alpha(s)\right) \tag{2.4}$$

The overall simulated brightness temperature is thus expressed as:

$$T_B = T_{BU} + \tau(ET_s + T_{B\Omega}) \tag{2.5}$$

where T_{BU} is the up-welling radiation of the atmosphere, τ is the total transmittance from the surface to the top of the atmosphere, E is the Earth surface emissivity, T_s is the physical temperature of the mixed surface of water and ice (including both multi-year ice and first-year ice), and $T_{B\Omega}$ is the scattered sky radiation.

Therefore, given the surface temperature T_s and the absorption coefficient at any position in the atmosphere, T_{BU} and T_{BD} can be computed. However, in practice, such an approach is not feasible since it requires determining T_s and α over the entire volume of the atmosphere. To simplify the computation, the atmospheric parameters are assumed to be horizontally uniform, which means, the absorption α is only a function of the altitude h above the surface, i.e. $\alpha(s) = \alpha(h)$. Hence the total transmittance is written as:

$$\tau(h_1, h_2, \theta) = \exp\left(-\sec(\theta)\int_{h_1}^{h_2} \mathrm{d}s\, \alpha(s)\right) \tag{2.6}$$

where θ is the incident angle of the satellite.

And the up-welling atmosphere radiation is given by:

$$T_{BU} = \sec(\theta)\int_0^H \mathrm{d}h\, \alpha(h)T(h)\tau(h, H, \theta) \tag{2.7}$$

The key component of the atmosphere model is the total transmittance τ from the surface to the top of the atmosphere that determines how much radiation is attenuated. In the microwave spectrum below 100 GHz, the vertically integrated atmosphere absorption is due to three components: oxygen, water vapour and liquid water path. The oxygen absorption is nearly constant globally, with a dependence on the air temperature, which is small at the atmospheric window frequencies of AMSR-E. The water vapour absorption is a linear function of the water vapour paths with a small second order term. And the final component liquid water absorption is approximated to be linear to the product of average cloud temperature and liquid water path (Wentz and Meissner, 2000).

The ocean-surface model consists of two parts. One is the dielectric constant of sea water that determines the emissivity and reflectance of the specular ocean. It is a complex number that depends on frequency ν, water temperature T_{water}, and water salinity s. The other component model is the wind roughened sea surface, since the microwave emission from the ocean also depends on the surface roughness. Three scales of waves are responsible for the variation of surface emissivity: the surface waves with wavelengths that are long compared to the radiation wavelength, the sea foam, and the surface waves that are small compared to the radiation wavelength (Wentz and Meissner, 2000).

The atmospheric parameters used in the Wentz forward model to simulate brightness temperatures are: columnar total water vapour(TWV), wind speed (WS), liquid water path (LWP) and surface temperature of ice and ocean. Apart from that, information about the total sea ice concentration and the fraction of multi-year ice are required as well.

2.3 Steps of Atmospheric Correction

The atmospheric correction is carried out in several steps shown in Figure 2.3. As described in Chapter 2.2, the brightness temperature measured by satellite antenna is contributed by the surface microwave emission and the atmosphere. The atmospheric correction is indeed a process to separate the surface thermal emission from the atmosphere contribution. Therefore, the first step of correction is to simulate the brightness temperature without atmosphere influence ($TBM0$). Here we assume the reference surface temperature of water and ice to be 0 ℃ (273.16 K), and all atmosphere parameters TWV, WS, LWP are zero as well. In reality, ice starts to melt at 0 ℃. In future work the ice temperature will be changed into -1.8 ℃. Secondly, the simulated brightness temperature with single

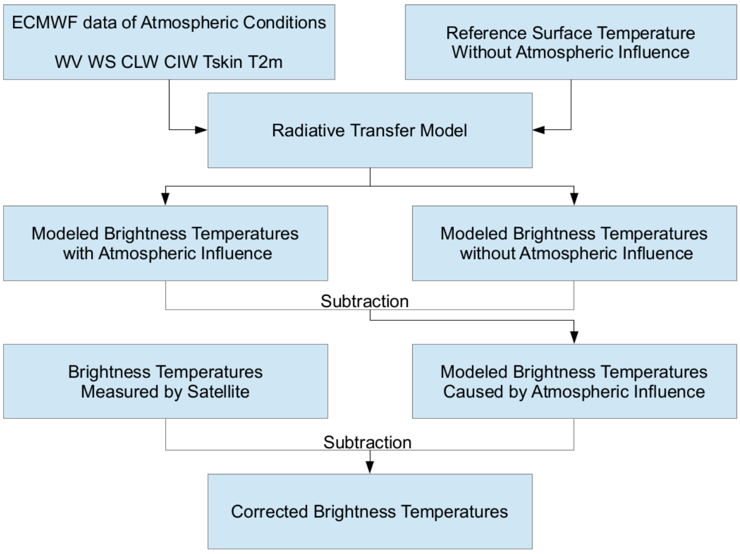

FIGURE 2.3: Flow chart of atmospheric correction steps. The key step is to simulate the brightness temperatures with and without atmospheric influence using the Wentz forward model.

or combined atmospheric influences (*TBMA*) are computed. For each correction, only the chosen atmospheric parameters (one or several at a time) are set to the collocated geophysical values from the reanalysis product, while all the other parameters are set to zero. Assuming that the contribution of atmosphere and surface emission to the measured brightness temperature is linear, the difference between *TBMA* and *TBM0* is thus regarded as the atmospheric contribution to the measured brightness temperature, and is in the end subtracted from the satellite measurement. The corrected brightness temperatures (*TBC*) is given as:

$$TBC = TB - (TBMA - TBM0) \tag{2.8}$$

where: *TBC* is the corrected brightness temperature, *TB* is the brightness temperature measured by satellite radiometer, *TBMA* is the brightness temperature modelled by collocated geophysical states, *TBM0* is the brightness temperature modelled without atmospheric influence.

2.4 Criteria of the Atmospheric Correction Effect

In order to evaluate the effect of the atmospheric correction, we test the correction on two validated data sets described in Chapter 2.1: the open water sites (SIC 0) and the fully ice-covered sites (SIC 1). Ideally, on the surface where the total ice concentration and the fraction of each ice type are all known, under certain surface temperature and with no atmospheric impact, the emitting temperature of ice and water should remain constant. In reality, due to the atmosphere, the observed brightness temperature has fluctuations. For the usually snow-covered sea ice, the Weddell Sea winter experiments show a standard deviation of 2.5 K (Comiso et al., 1989) of the ice-emitting temperature. For ocean surface, such fluctuation is more pronounced because the atmosphere has more influence on the emissivity of water. As explained in Chapter 2.2, the total transmittance of the atmosphere is a key component of how much surface microwave emission is attenuated before reaching the radiometer, hence the variation of atmospheric constituents like water vapour, cloud liquid water would also increase the fluctuation of detected brightness temperature. Thus, after such atmospheric impact is corrected, we expect a much narrower distribution of the measured brightness temperature, or in other words, a smaller standard deviation. The correction that results in the least standard deviation of T_{BH}, T_{BV} and P (polarization difference) at 89 GHz is considered to be the best correction. The corrected brightness temperatures derived from the best correction are then used to retrieve total ice concentration.

2.5 Sea Ice Retrieval Algorithms

After selecting the best atmospheric correction, the resulting corrected brightness temperatures are adapted to retrieve total ice concentration using a non-linear algorithm: ASI, and a linear algorithm: Linear 90 (Lin90), both using the same set of tie points derived from TBC, and the result of which is compared to the SIC retrieved by ASI using standard tie points. Also, during the process of atmospheric correction, another two algorithms are used to compute the preliminary total ice concentration and fraction of each ice type: the NASA Team and the ECICE Algorithm. In this section, all involved ice concentration retrieval algorithms are explained in detail.

2.5.1 Artist Sea Ice Algorithm

The Artist Sea Ice algorithm, ASI in short, is the core ice retrieval algorithm of this study. It is an enhancement of the Svendsen sea ice algorithm for near 90 GHz frequencies (Svendsen et al., 1987), developed to benefit from the high spatial resolution of the 85 GHz channels of the SSM/I sensors for analysing the mesoscale ocean-atmosphere interaction (Kaleschke et al., 2001). The total ice concentration is calculated from the polarization difference P of the brightness temperatures T_B,

$$P = T_{B,V} - T_{B,H} \tag{2.9}$$

where V denotes vertical and H horizontal polarization. Near 90 GHz, the polarization difference of emissivity is similar for both first-year and multi-year ice and is much smaller than open water (Figure 1.1). This holds for polarization difference of brightness temperature P as well, since the physical temperature is identical for both $T_{B,V}$ and $T_{B,H}$, and thus only emissivity differences influence P. Consider the atmospheric impact a_c on the polarization difference, we have:

$$P = P_s a_c \tag{2.10}$$

where $a_c = e^{-\tau}(1.1e^{-\tau} - 0.11)$, according to the Svendsen algorithm (Svendsen et al., 1987). This approximation is valid for a horizontally stratified atmosphere with an effective physical temperature instead of the vertical temperature profile, and a diffusely reflecting surface viewed at an incidence angle of about 50°.

The surface polarization difference P_s is contributed by ice and open water:

$$P_s = CP_{s,ice} + (1-C)P_{s,water} \tag{2.11}$$

where $P_{s,ice}$ and $P_{s,water}$ are surface polarization difference for ice and water, respectively. Thus P becomes a function of the total ice concentration:

$$P(C) = (CP_{s,ice} + (1-C)P_{s,water})\, a_c. \tag{2.12}$$

Svendsen (Svendsen et al., 1987) found that the atmospheric influence a_c is in general a function of total ice concentration. Thus derived from equation (2.12), the polarization difference for $C = 0$ (open water) and $C = 1$ (closed ice cover) are given by:

$$P_0 = a_0 P_{s,water} \tag{2.13}$$

$$P_1 = a_1 P_{s,ice} \tag{2.14}$$

Applying Taylor expansions to equation (2.12) around $C = 0$ and $C = 1$, neglecting all higher terms, assuming that the derivatives of the atmospheric influence $a_0\prime$ and $a_1\prime$ are both zero and that the atmospheric influence over open water and closed ice are nearly identical, then rearranging the equations as a function of total sea ice, we get:

$$C = \left(\frac{P}{P_0} - 1\right)\left(\frac{P_{s,water}}{P_{s,ice} - P_{s,water}}\right) \qquad for\, C \to 0 \tag{2.15}$$

$$C = \frac{P}{P_1} + \left(\frac{P}{P_1} - 1\right)\left(\frac{P_{s,water}}{P_{s,ice} - P_{s,water}}\right) \qquad for\, C \to 1 \tag{2.16}$$

where $P_{s,water}/(P_{s,ice} - P_{s,water}) = -1.14$ is a typical value for sea ice signature under Arctic conditions (Svendsen et al., 1987). To retrieve ice concentration in regions of intermediate concentrations, we assume that the variation of the atmospheric effects is a smooth function of C and interpolate between equations (2.15) and (2.16) with the third order polynomial:

$$C = d_3 P^3 + d_2 P^2 + d_1 P + d_0. \tag{2.17}$$

The unknown coefficients d_i can be determined by the linear equation system:

$$\begin{bmatrix} {P_0}^3 & {P_0}^2 & P_0 & 1 \\ {P_1}^3 & {P_1}^2 & P_1 & 1 \\ 3{P_0}^3 & 2{P_0}^2 & P_0 & 0 \\ 3{P_1}^3 & 2{P_1}^2 & P_1 & 0 \end{bmatrix} \begin{bmatrix} d_3 \\ d_2 \\ d_1 \\ d_0 \end{bmatrix} = \begin{bmatrix} 0 \\ 1 \\ -1.14 \\ -0.14 \end{bmatrix} \tag{2.18}$$

And thus the total ice concentration can be calculated by equation (2.17). Note that the solution of the above linear equation system only depends on the polarization difference of open water P_0 and of fully ice covered surface P_1. P_0 and P_1, so called tie points, are empirical values of the radiometric signature of ice free and closed ice under typical condition of the investigated region. Tie points can be chosen as dynamical or constant values according to the time and region span of the study. A careful choice of tie points (P_1 and P_0) is essential for a correct ice retrieval. For the near real time ice maps produced daily by *PHAROS* group (Physical Analysis of Remote Sensing Images), the tie points are chosen as $P_1 = 11.7$ K, $P_0 = 47$ K (Spreen et al., 2008), which also include the average atmospheric influence. Constant tie points are used here to achieve a large continuous global ice concentration time series. Equation (2.17) then becomes:

$$C = 1.64 \cdot 10^{-5} P^3 - 0.0016\, P^2 + 0.0192\, P + 0.9710\,. \tag{2.19}$$

For all P greater than P_0 or lesser than P_1, the corresponding ice concentration is 0% or 100% respectively. Figure 2.4 illustrates the relationship between *C(ASI)* and the polarization difference P. The blue polynomial displays the *C(ASI)* as a function of P. The red dashed line shows the ice concentration as a linear function of P determined by the tie points P_1 and P_0 marked by the green and magenta vertical lines respectively. We call this algorithm *Lin90*. The discrepancy between *C(ASI)* and *C(Lin90)* is negligible at *SIC* lower than 30%, increases slowly by 10% at $P = 25$ K, then drops back to zero at $C = 100\%$.

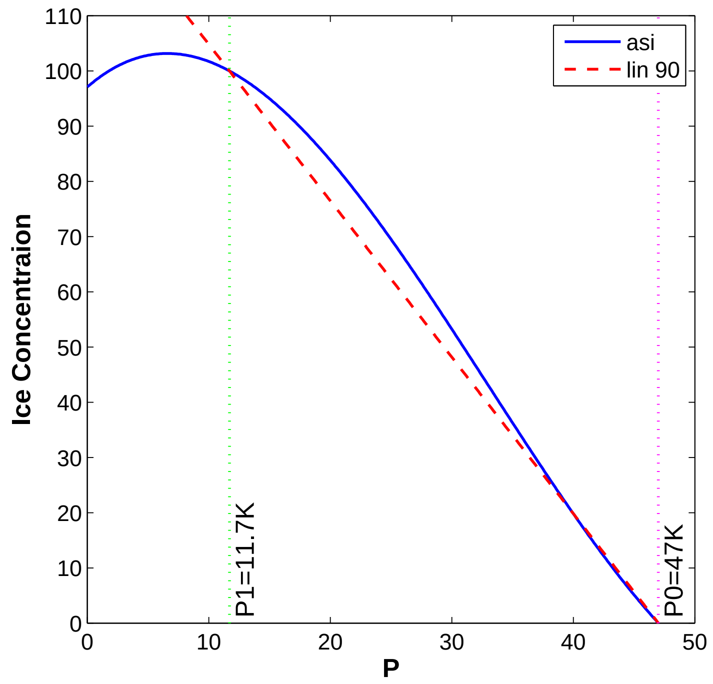

FIGURE 2.4: Ice concentration C as a function of polarization difference P. The blue curve is the *ASI* curve using standard tie points, $P_0 = 11.7\ K$, $P_1 = 47\ K$, marked by the green and magenta vertical lines respectively. The dashed red line illustrates the *Lin90* algorithm using the same set of tie points. The difference between *C(ASI)* and *C(Lin90)* is more pronounced at high ice concentration, resulting a more stable retrieval at high ice concentrations.

At 89 GHz, high cloud liquid water over open ocean can reduce the polarization difference to values similarly small as those of sea ice. Study (Fuhrhop et al., 1998) shows that high cloud liquid water over ice leads to a shift from first-year ice to multi-year ice. Therefore weather filters are adopted to avoid those more pronounced atmospheric influence on the brightness temperatures. The first weather filter uses the gradient ratio (GR) of the 36.5 and 18.7 GHz channels and mainly filters high cloud liquid water cases:

$$GR(36.5/18.7) = \frac{T_B(36.5V) - T_B(18.7V)}{T_B(36.5V) + T_B(18.7V)} \tag{2.20}$$

For $GR(36.5/18.7) \geq 0.045$, $C(ASI) = 0$ according to (Spreen et al., 2008).

The second weather filter is the gradient ratio $GR(23.8/18.7)$ to screen out high total water vapour cases. For $GR(23.8/18.7) \geq 0.04$, $C(ASI) = 0$ (Spreen et al., 2008).

In case the two weather filters do not screen out all anomalies, the Bootstrap algorithm is used to confirm 0% ice concentration:

$$C(Bootstrap) = 0 \Rightarrow C(ASI) = 0. \tag{2.21}$$

Henceforth, we call this version of *ASI* that include two weather filters and the *Bootstrap* filter as *ASI_Bootstrap* algorithm. The spatial resolution of *ASI_Bootstrap* is determined by the coarsest frequency channel, i.e. 18.7 GHz with 16×27 km^2 resolution for AMSR-E, and thus the high resolution advantage of 89 GHz is lost. To make up for that, the resulting ice concentration is interpolated into the high resolution grid. During this process, the atmospheric influences are averaged over the coarsest grid, which could lead to misclassification of ice as open water.

In Chapter 4, a new set of tie points will be chosen for the corrected brightness temperatures, leading to a new version of equation 2.17 with different coefficients. All the weather filters used in *ASI_Bootstrap* are replaced by atmospheric correction based on the collocated geophysical states. This new version of *ASI* will be referred as *ASI2*. Details of *ASI2* are explained in Chapter 4.

2.5.2 NASA Team Algorithm

Developed in 1985,the NASA Team (NT) algorithm (Swift et al., 1985) estimates the fractions of first-year and multi-year sea ice types by using three microwave radiometer channels: 19 GHz vertically (V) and horizontally (H) polarized channels and the vertically polarized 37 GHz channel. Two independent variables are used in the algorithm: the polarization (PR) and spectral gradient ratios (GR) defined by:

$$PR(19) = \frac{T_B(19V) - T_B(19H)}{T_B(19V) + T_B(19H)} \tag{2.22}$$

$$GR(37/19) = \frac{T_B(37V) - T_B(19V)}{T_B(37V) + T_B(19V)}. \tag{2.23}$$

From these two variables, the concentrations of first-year ice and multi-year ice are given by:

$$C_FY = (a_0 + a_1PR + a_2GR + a3PR \cdot GR)/D \tag{2.24}$$

$$C_MY = (b_0 + b_1PR + b_2GR + b3PR \cdot GR)/D \tag{2.25}$$

$$D = (c_0 + c_1PR + c_2GR + a3PR \cdot GR). \tag{2.26}$$

a_i, b_i, c_i are functions of a set of tie points (in the form of brightness temperatures) of the surface types of open water, first-year and multi-year ice.

2.5.3 Environment Canada Ice Concentration Extractor Algorithm

In 2007, the Canadian Ice Service (CIS) developed a new method called Environment Canada Ice Concentration Extractor (ECICE) to retrieve the total ice concentration and partial concentration of three ice types: new ice, young ice and first-year ice. ECICE adopts two important concepts. One is a mathematical optimization technique to determine the best ice type concentrations from multi-channel radiometric observations compatible with the observed brightness temperatures. In this study we use the brightness temperatures at both polarizations of the 19 GHz and 37 GHz channels. Secondly, ECICE adopts a distribution of characteristic values of a radiometric parameter (brightness temperatures and, in some versions also microwave backscatter coefficients) that represents an ice type or open water instead of using single tie point.

Chapter 3

Effect of Atmospheric Correction on Brightness Temperatures

3.1 Distribution of Brightness Temperatures

In this section, we briefly introduce the range of brightness temperatures of our validation datasets, and explain the difference of distribution over ice free and fully ice covered surface, to get an impression of the typical T_Bs in the Arctic.

3.1.1 0% Ice Concentration

The satellite measured brightness temperatures at 89 GHz range from 160 K to about 280 K at both polarizations over open water. Figure 3.1 shows the histogram of the horizontally and vertically polarized brightness temperatures (T_{BH} and T_{BV}) and the polarization difference (P) over ice free surface before the atmospheric correction. T_{BH} is more evenly distributed between 160 K and 270 K, with the mean value of 207.6 K and standard deviation of 19.4 K. The distribution of T_{BV} is much narrower, which ranges from 235 K to 275 K, having an average value of 248.9 K, and a much lower standard deviation of 7.4 K. The significant difference in polarizations indicates that the microwave radiation of open ocean is highly polarized. The mean polarization difference over ice free ocean is 41.4 K, and its standard deviation is 12.7 K.

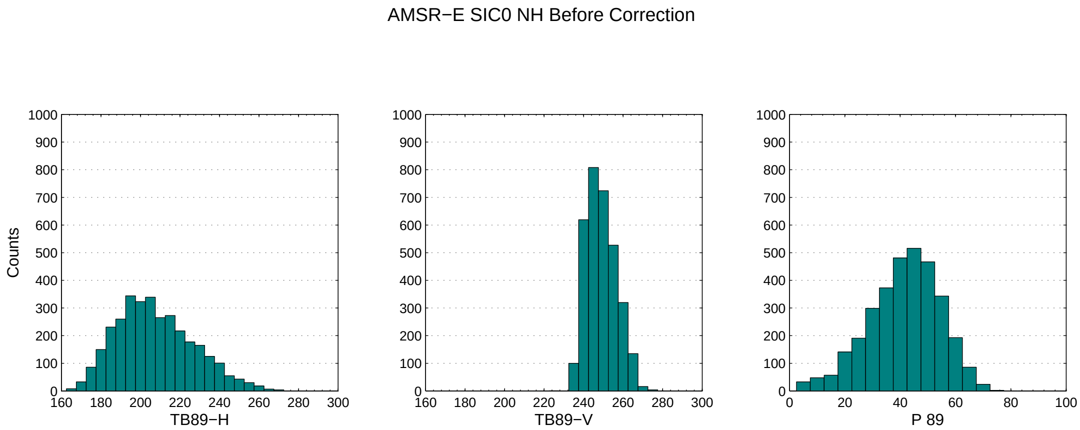

FIGURE 3.1: The histograms of AMSR-E observed brightness temperatures at H- and V- polarizations, and the polarization difference P, over open water in the Arctic before the atmospheric correction. The bin size is 5 K for all three plots.

3.1.2 100% Ice Concentration

The AMSR-E measured brightness temperatures at 89 GHz of the fully ice covered research regions vary from 150 K to 280 K. As shown in the histograms of the brightness temperatures at both polarizations (Figure 3.2), the difference between the two polarizations is small. The mean value of the horizontal polarized brightness temperatures is 202.8 K with the standard deviation of 19.6 K. The average vertically polarized brightness temperature is slightly higher, 212.6 K, and the standard deviation is 20.7 K. The corresponding polarization difference range from 5 K to 25 K, with a low standard deviation of 2.8 K. The small polarization difference is consistent with the fact that the radiation emitted by ice is less polarized than that of open water.

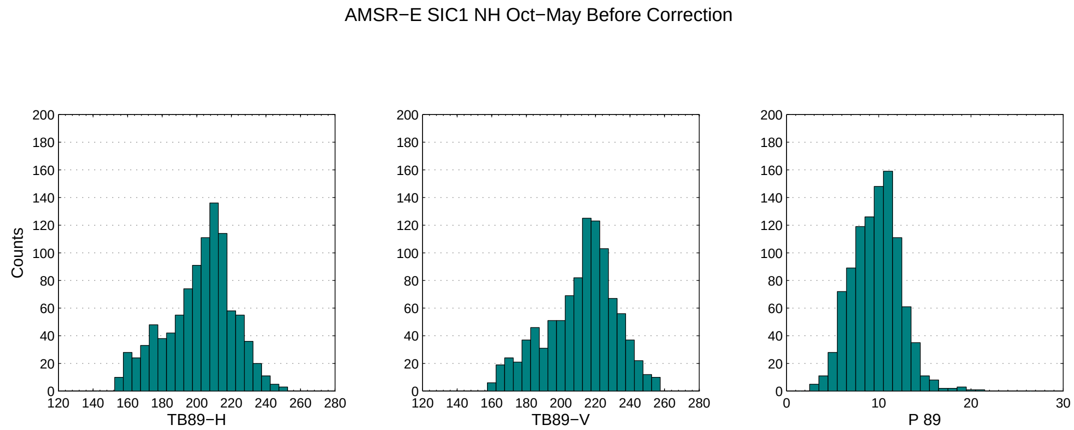

FIGURE 3.2: The histograms of AMSR-E observed brightness temperatures at H- and V- polarizations, and the polarization difference P, over closed ice in the Arctic before the atmospheric correction. The bin size is 5 K for T_{BH} and T_{BV}, and 1 K for P .

3.2 Sensitivity of Brightness Temperatures to Geophysical Parameters

For the actual correction, it is required to estimate the atmospheric influence on the observed brightness temperatures. In this section, a sensitivity study of the measured brightness temperatures to geophysical parameters is implemented to assess the atmospheric impact on brightness temperatures of open water and closed ice.

3.2.1 0% Ice Concentration

In order to evaluate the influence of atmosphere to measured brightness temperatures, T_{BH} and T_{BV} are simulated with varying geophysical parameters of typical values under the Arctic condition. Figure 3.3 shows the sensitivity of brightness temperatures over open water to the chosen atmospheric parameters: *WS*, *TWV*, *LWP* and T_s, each represented by a different colour. The solid lines indicate the variability of vertically polarized T_Bs with the atmospheric parameter of the corresponding colour, while the dashed lines denote that of the horizontally polarized T_Bs. In general, the variability of T_Bs with most parameters is nearly linear in

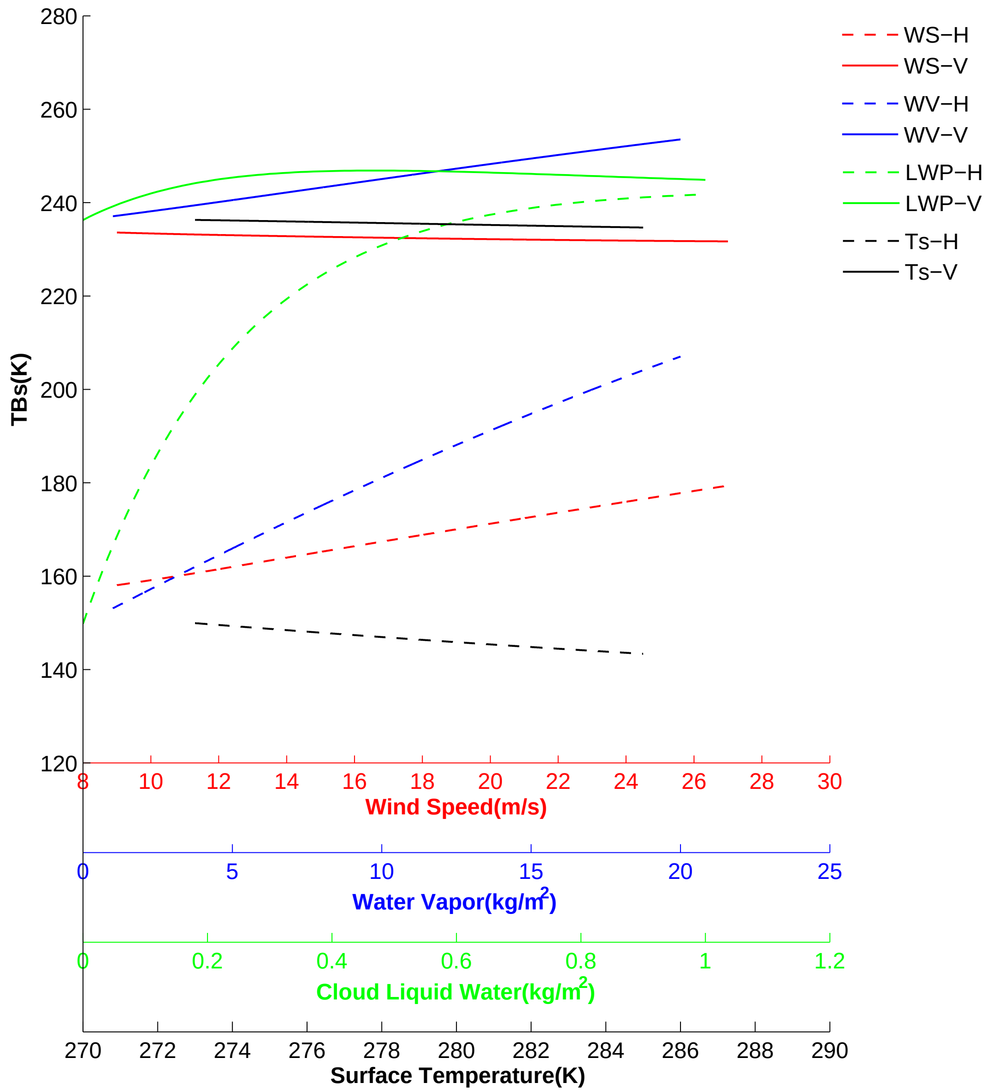

FIGURE 3.3: The sensitivity of T_Bs to the chosen geophysical parameters over open water: *WS*, *TWV*, *LWP* and T_s, each represented by a different colour. The solid lines indicate the variability of vertically polarized T_Bs with the atmospheric parameter of the corresponding colour, while the dashed lines denote that of the horizontally polarized T_Bs.

the considered range, except for *LWP*. The polarization difference is observed to decrease with all increasing parameters but for the surface temperature.

The wind speed of the researched regions varies from 0 to 28 m/s, with the average value 9.03 ± 4.14 m/s. Over open water, wind causes roughened sea surface and results in higher emitting emissivity. Therefore T_Bs are expected to increase with wind speed. However, as shown by the red lines in Figure 3.3, T_Bs decrease slightly with increasing wind speed at vertical polarization. This could be caused by the mixing of polarizations. The emission from a calm sea surface is highly polarized. When strong wind occurs, the thus roughened surface would have higher emissivity and be less polarized in the vertical direction (Wentz and Meissner, 2000). That is to say, though the overall emissivity is higher over roughened ocean surface, due to the mixing of polarizations, emissivity increases at horizontal while decreases at vertical direction.

The Arctic often has very low humidity. Among all the selected regions, the total water vapour of over 80% data points is below 15 kg/m^2. The maximum value is about 40 kg/m^2, while the average TWV is 9.98 ± 5.22 kg/m^2. The simulated T_Bs increase with TWV as expected at both 89-H and 89-V, shown by the blue lines in Figure 3.3. The increase at horizontal polarization is stronger than that at vertical, which leads to a strong drop in polarization difference from approximately 80 K (at $TWV = 0$ kg/m^2) to 50 K (at $TWV = 20$ kg/m^2). In the ASI algorithm, the retrieved ice concentration depends on the polarization difference at 89 GHz. The currently used tie points are $P_0 = 47$ K (open water) and $P_1 = 11.7$ K (closed ice), i.e. the surface is classified as open water if the polarization difference is larger than P_0, is fully ice covered if P is smaller than P_1, and is partially covered by ice if P is between P_1 and P_0. Therefore under typical polar atmospheric conditions ($TWV < 15$ kg/m^2), with the influence of TWV alone, open water won't be misclassified as partially ice covered surface despite the decrease in polarization difference.

Clouds change the polarization (PR) and spectral gradient ratio (GR), and thus causes shift in the retrieval of sea ice types (Fuhrhop et al., 1998).Over closed ice, liquid water causes a shift from multi-year ice to first-year ice, and snow clouds have the opposite effect. According to their constituent, clouds are classified into two types: ice and liquid water clouds. Only liquid water clouds are considered in the Wentz forward model because they have a stronger interaction with microwaves, due to the higher dielectric constant of liquid water than ice. In the investigated regions, the LWP of over 80% data is below 0.1 kg/m^2 resulted from the low humidity in the Arctic. Its mean value is 0.06 ± 0.1 kg/m^2, which indicates a high relative variability. Among all tested atmospheric parameters, LWP has the most non-linear influence on measured T_Bs. The polarization difference drops strongly from around 80 K (at $LWP = 0$ kg/m^2) to 45 K (at $LWP = 0.25$ kg/m^2), lower than the standard tie point $P_0 = 47$ K. This explains the abnormally low polarization difference of some data points in the SIC 0 data set. Among the some 3000 data sets, the polarization difference of approximately 200 data points is below 20 K. Most of those data have both high TWV and LWP. Without weather filter or atmospheric correction, those regions will be misclassified as partially ice covered surface by the ASI algorithm.

Opposed to our expectation, the simulated brightness temperatures decrease with the surface temperature. As explained in Section 2.2, the simulated T_Bs are combined microwave emissions from the surface and the atmosphere, both attenuated by the atmosphere. If given the same atmospheric conditions, the atmospheric emission and absorption should remain the same, and thus the modelled T_Bs only depend on the surface temperature and surface emissivity. Hence we deduce the drop of T_Bs is caused by the variation of emissivity. The emissivity of saline water is mainly determined by the dielectric permittivity ϵ, which defines how the molecules interact with the electromagnetic radiation. For distilled water, the dielectric constant ϵ decreases exponentially with the surface temperature. For saline water, the effect of ionic conductivity is added (Klein and Swift, 1977). The dielectric constant of saline water is defined by the Debye equation (Wentz and Meissner, 2000):

$$\epsilon = \epsilon_\infty + \frac{\epsilon_0 - \epsilon_\infty}{1 + j[\lambda_R/\lambda]^{(1-\eta)}} - \frac{2j\sigma\lambda}{c} \tag{3.1}$$

where ϵ_∞ is the dielectric constant of water at infinite frequency; λ_R is the relaxation wavelength; λ is the wavelength of the radiation; η is the spread factor, an empirical parameter that describes the distribution of the relaxation wavelengths; σ is the ionic conductivity of salt water; and c is the speed of light. The dielectric constant of saline water at zero frequency ϵ_0 depends on the salinity and the ocean surface temperature. The measurement of the salinity dependence of ϵ_0 is usually carried out at low frequencies such as 2.65 GHz (Saxton, 1952) and 1.4 GHz (Ho and Hall, 1973). In the Wentz forward model, the dielectric constant model of saline water is similar to Klein and Swift (1977), in which the salinity dependence of ϵ_s is measured at 1.4 GHz. Based on this model, the real part of the dielectric permittivity ϵ of ocean water with the salinity 35‰ increases with the ocean surface temperature (see Figure 3.4). The imaginary part of the dielectric constant is related to the dissipation of energy within water, and does not influence the reflectance. Therefore the imaginary part is not taken into account. With the dielectric constant known, the reflectivities ρ_H and ρ_V are computed using the Fresnel equations:

$$\rho_V = \frac{\epsilon \cos\theta_i - \sqrt{\epsilon - \sin^2\theta_i}}{\epsilon \cos\theta_i + \sqrt{\epsilon - \sin^2\theta_i}} \tag{3.2}$$

$$\rho_H = \frac{\cos\theta_i - \sqrt{\epsilon - \sin^2\theta_i}}{\cos\theta_i + \sqrt{\epsilon - \sin^2\theta_i}}, \tag{3.3}$$

where θ_i is the incident angle. In this study, the incident angle is that of AMSR-E, i.e. 55°. The reflectivity R of calm ocean is thus defined as:

$$R_P = |\rho_P|^2 \, . \tag{3.4}$$

Under windless condition, assuming the ocean surface is strictly specular, its emissivity is then:

$$E = 1 - R_P \, , \tag{3.5}$$

where the subscript P denotes polarization.

Given the emissivities and the surface temperatures, the emitted brightness temperature of the sea surface can be computed at any frequency, salinity and incident angle. A sensitivity study of the brightness temperature T_B and the surface physical temperature T_s is done at the microwave spectrum for brine water with the salinity of 35‰ and incident angle 55°. The sea surface temperature sensitivity Q_{T_s} is defined as dT_B/dT_s. Figure 3.5 shows the spectral variation of Q_{T_s} between

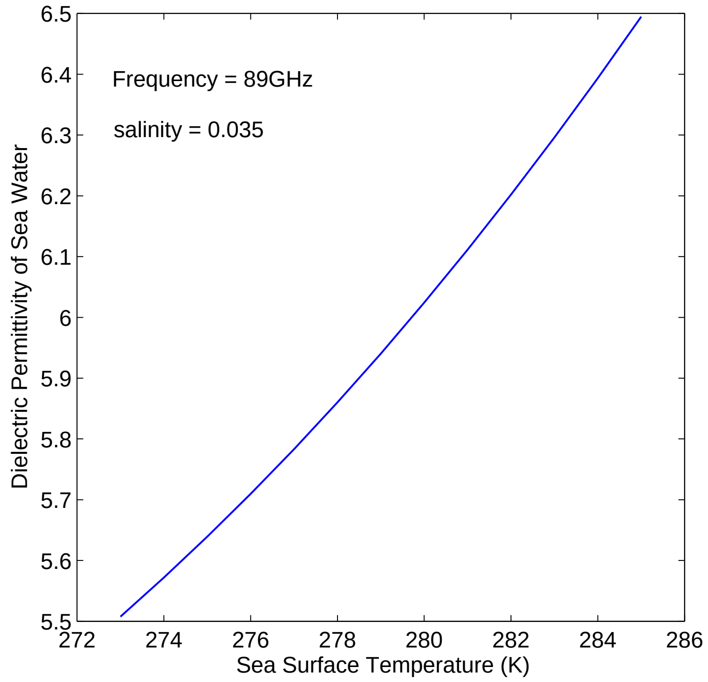

FIGURE 3.4: The sensitivity of ocean dielectric constant ϵ to sea surface temperature T_s based on the study of Swift in 1977(Klein and Swift, 1977).

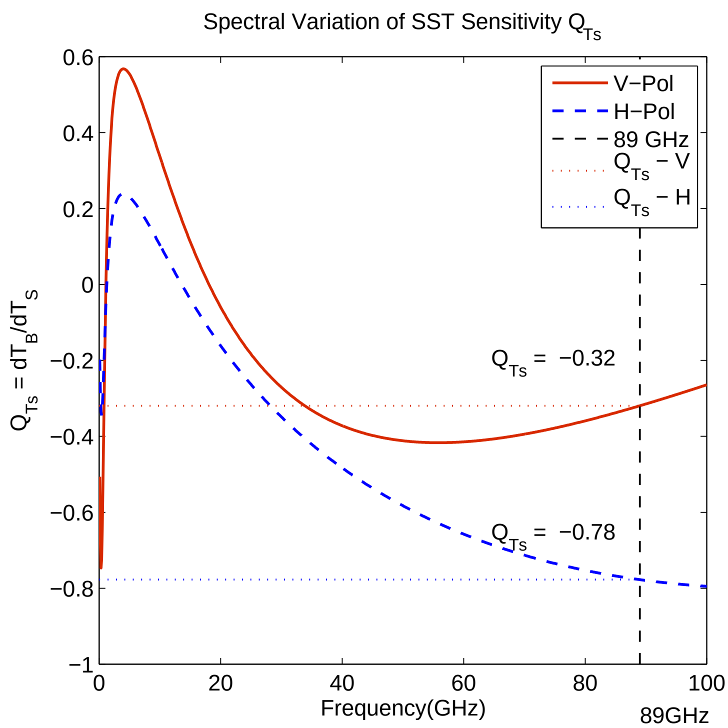

FIGURE 3.5: The spectral variation of sea surface temperature sensitivity Q_{T_s} at microwave spectrum between 0 and 100 GHz. Red curve denotes vertical polarization, and blue for horizontal. Q_{T_s} is defined as $dT_B/dT_{surface}$. At 89 GHz, Q_{T_s} is negative at both polarizations.

0 GHz and 100 GHz. At low frequencies, for both polarizations the sensitivity Q_{T_s} increase rapidly from negative to positive values and reach the maximum at ca.5 GHz. The sea surface temperature sensitivity Q_{T_s} of horizontal polarization decrease slowly from 5 GHz, turn to zero at approximately 12 GHz, and continue decreasing until 100 GHz. The Q_{T_s} of vertical polarization first decrease from 5 GHz, reach zero at about 20 GHz, and then slowly rise again from 50 GHz until 100 GHz but still remains negative. Q_{T_s} of vertical polarization is higher than that of horizontal at all tested frequencies. At our desired frequency 89 GHz, the sensitivity Q_{T_s} is -0.32 at 89-V, and -0.78 at 89-H. Note that the sensitivity of brightness temperature to surface temperature of open water (the slope of black lines in Figure 3.3), which are -0.14 and -0.55 at vertical and horizontal polarization respectively, are lower than the corresponding Q_{T_s} in absolute values. The difference is due to atmospheric attenuation. While computing Q_{T_s}, only the emitting brightness temperature is considered, unlike the simulated T_Bs where the atmospheric influence is also included.

Among the chosen ERA-Interim geophysical products, both 2 meters air temperature T_{2m} and skin temperature T_{skin} are related to surface temperature. As described in the ERA-Interim Archive (Berrisford et al., 2011), skin temperature is the temperature of the atmosphere - Earth interface. The 2 meters air temperature is strongly correlated with skin temperature and total water vapour content as shown in the scatter plot Figure 3.6. The black line is the linear fit of T_{2m} to T_{skin}. Different colours indicate the corresponding total water vapour TWV. In general, T_{2m} is lower than T_{skin}, while with T_{2m} exceeding skin temperature, TWV also increases. As the T_{2m} raises from 265 K to 270 K, the corresponding skin temperature remains almost constant at 275 K, because as the air temperature varies, the ice surface takes some time to change its temperature accordingly.

3.2.2 100% Ice Concentration

According to its role in the radiative transfer model, the atmospheric influences have two types: atmospheric properties (TWV, LWP) and surface properties (WS,

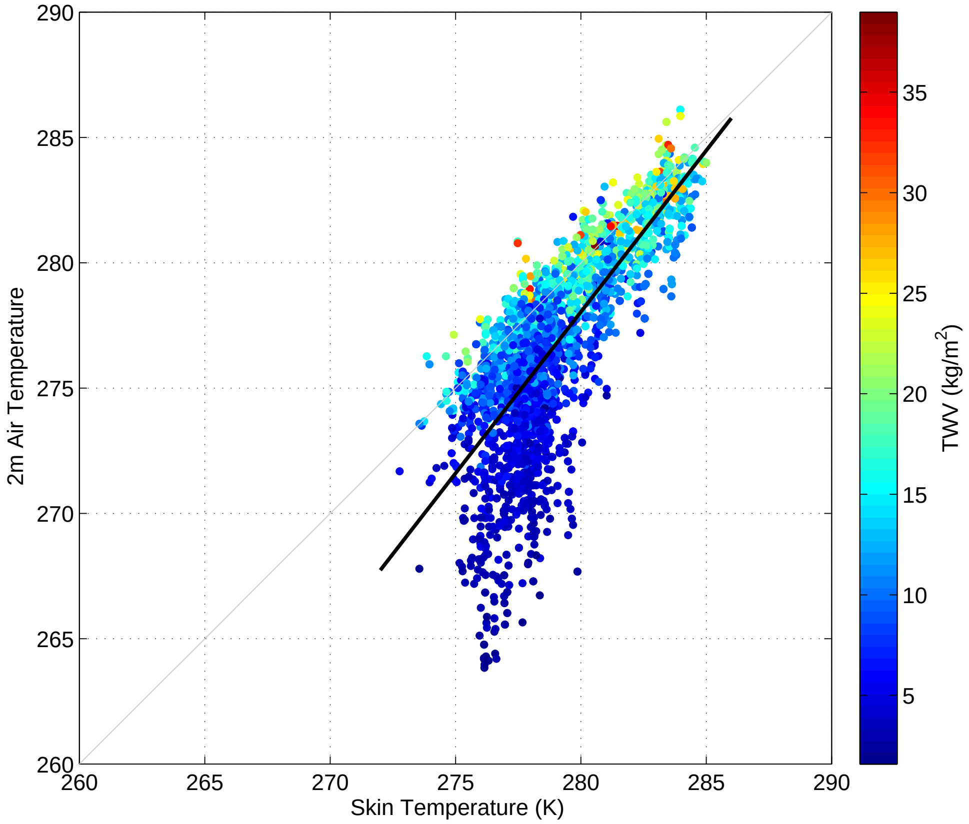

FIGURE 3.6: Scatter plot of T_{2m} to T_{skin} in the Arctic over open water. The data is from all months in 2008, produced by ERA-Interim. The colour of the dots indicates the corresponding total water vapour value. The black line is the linear fit of the scatter plot. The grey line is the reference line. In general, T_{2m} is lower than T_{skin}, and it may exceed T_{skin} when water vapour is above 15 kg/m^2.

T_{skin}, T_{2m}). The atmospheric properties impact the atmospheric attenuation by varying total water vapour, liquid water path, etc. The surface properties such as the roughness of ocean and surface temperature influence the emitting radiation by varying the physical temperature or the emissivity. Over open water, the surface properties is strongly influenced by wind speed, which changes the geometry of water surface and thus varies the emissivity. As for sea ice, surface properties mainly depend on the ice types due to their different emissivities. Figure 1.1 shows the emissivities of sea ice and water at AMSR-E frequencies. At 89 GHz, the emissivities of first-year ice are much higher that those of multi-year ice at both polarizations. However, the polarization difference in emissivities for both ice types is very low compared to that of open water. Therefore over an ice-covered surface with mixed ice types, more multi-year ice causes a lower surface emissivity. In the sensitivity study of brightness temperatures to varying atmospheric parameters over 100% ice, we assume the sea ice only consists of multi-year ice, and test the influence of multi year ice fraction as a separate parameter. Table 3.1 shows the emissivities of first-year ice and multi-year ice used in this sensitivity study (Mathew et al., 2009).

As presented in Figure 3.7, the atmospheric properties (*WS*, *TWV* and *LWP*) affect the fully ice covered surface in the same manner as affecting open water (see Figure 3.3), but has a much less impact due to the low concentration of total water vapour and liquid water path and to the high emissivity of ice. Among all the selected regions, the total water vapour of over 80% data points is below 5 kg/m^2. Its maximum value is about 15 kg/m^2, with the mean value of 3.1 ± 2.5 kg/m^2, much lower than that over open water. With increasing total water vapour, the simulated brightness temperatures at both polarizations rise nearly linearly in the tested range, and the polarization difference slightly decreases.

Fuhrhop et al. (1998) shows that thick liquid clouds induce shift from multi-year ice to first year ice in the retrieval of ice type. However, the *ASI* algorithm does not distinguish between different ice types. Based on that fact, together with the low average liquid water path (0.005 ± 0.016 kg/m^2) over the test ice covered regions, *LWP* has little impact on the simulated brightness temperatures as expected. Note that the range of *LWP* in the plot (green curves in Figure 3.7) is chosen to be between 0 and 1.5 kg/m^2, much larger than the actual range, to show the non-linear influence of *LWP* on the simulated brightness temperatures.

As shown in Figure 3.7, the simulated brightness temperatures remain practically constant with varying wind speed, and increase with surface temperatures at both polarizations. Since the emissivity of multi-year ice is much lower than that of first-year ice, with higher multi-year ice fraction, the overall emissivity decreases, resulting in lower simulated brightness temperatures.

TABLE 3.1: The emissivities of First- and Multi-Year ice at 89 GHz in dual polarizations, averaged over all months (Mathew et al., 2009).

	First-Year Ice	Multi-Year Ice
89-H	0.94	0.78
89-V	0.86	0.72

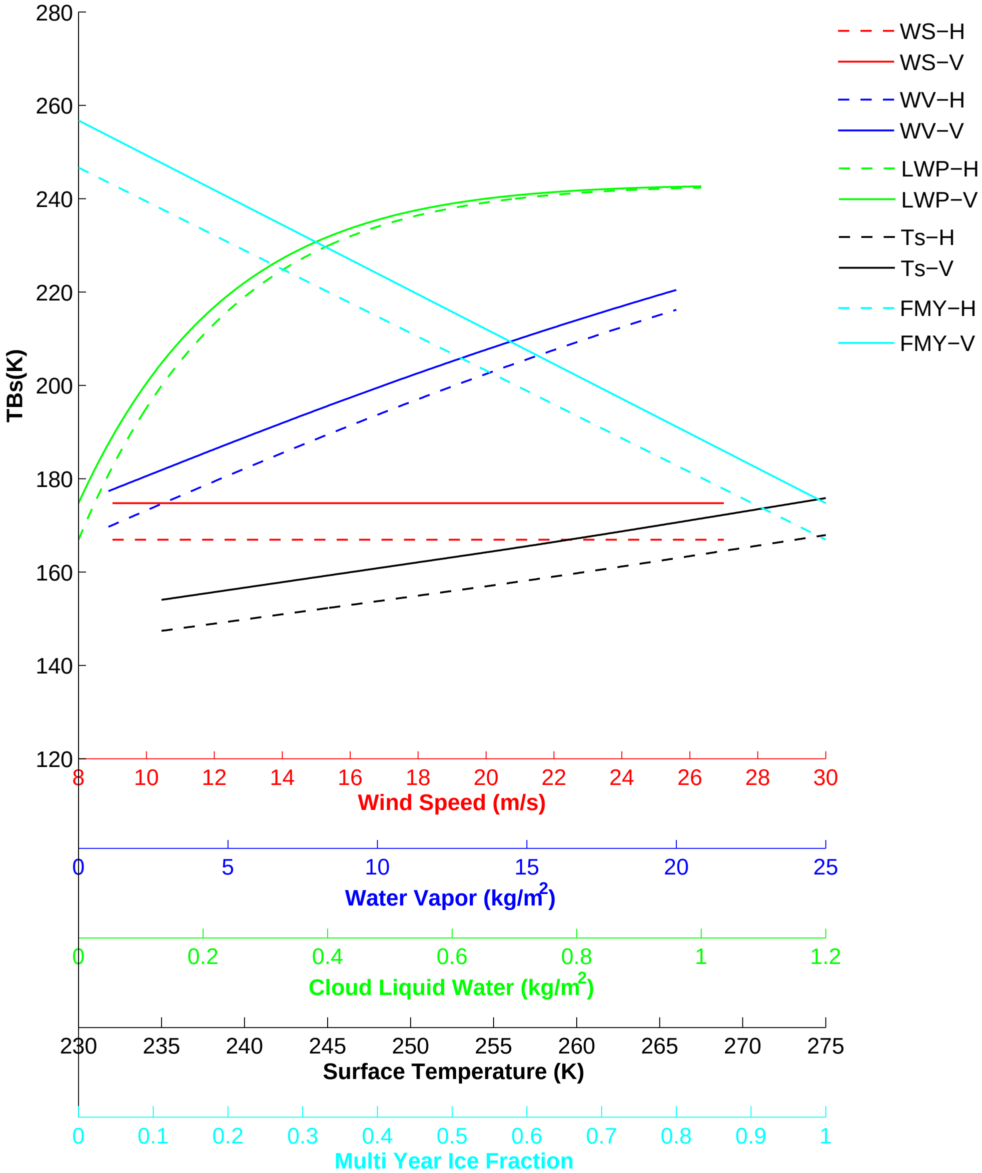

FIGURE 3.7: The sensitivity of T_Bs to the chosen geophysical parameters over closed ice: WS, TWV, LWP, T_s and multi-year ice fraction (FMY), each represented by a different colour. The solid lines indicate the variability of vertically polarized T_Bs with the atmospheric parameter of the corresponding colour, while the dashed lines denote that of the horizontally polarized T_Bs.

3.3 Effect of Atmospheric Correction on Brightness Temperatures

As explained in Chapter 2.4, an effective atmospheric correction causes reduction of the standard deviation of the brightness temperatures. To assess the effect of different atmospheric corrections, the standard deviations of the brightness temperatures std-T_Bs and of the polarization difference std-Ps are calculated before and after each correction. Both single and combined corrections based on all the involved atmospheric parameters are evaluated in this chapter.

3.3.1 0% Ice Concentration

All possible corrections (23 in total), including single and combined corrections, are applied to the test regions over open water at northern hemisphere from all seasons. The standard deviations of T_Bs at both polarizations before (red line for H-Pol and blue for V-Pol) and after (red bars for H-Pol and blue bars for V-Pol) are calculated, and displayed in Figure 3.8. The correction that causes the largest reduction in std-T_B is regarded as the most effective one.

Among the five single corrections: total water vapour, wind speed, cloud liquid water, T_{2m} and T_{skin} , TWV causes the least std-T_Bs after correction, from 19.4 K to 13.8 K at H-Pol and from 7.4 K to 4.6 K at V-Pol. The good performance of water vapour correction is consistent to the high sensitivity of T_Bs to total water vapour as explained in Figure 3.3. The influence of the correction for wind speed is small for both polarizations. The cloud liquid water correction results in a smaller reduction in std-T_Bs than water vapour despite the higher sensitivity of T_B to LWP. The T_{2m} and T_{skin} corrections both lead to a slight increase in std-T_Bs. Compared to TWV and LWP, the effect of the other three single corrections is negligible. The poor performance of wind speed, T_{2m} and T_{skin} is well explained by the low sensitivity of T_Bs to the corresponding parameters (see Figure 3.3). On the other hand, though having a high sensitivity, cloud liquid water correction

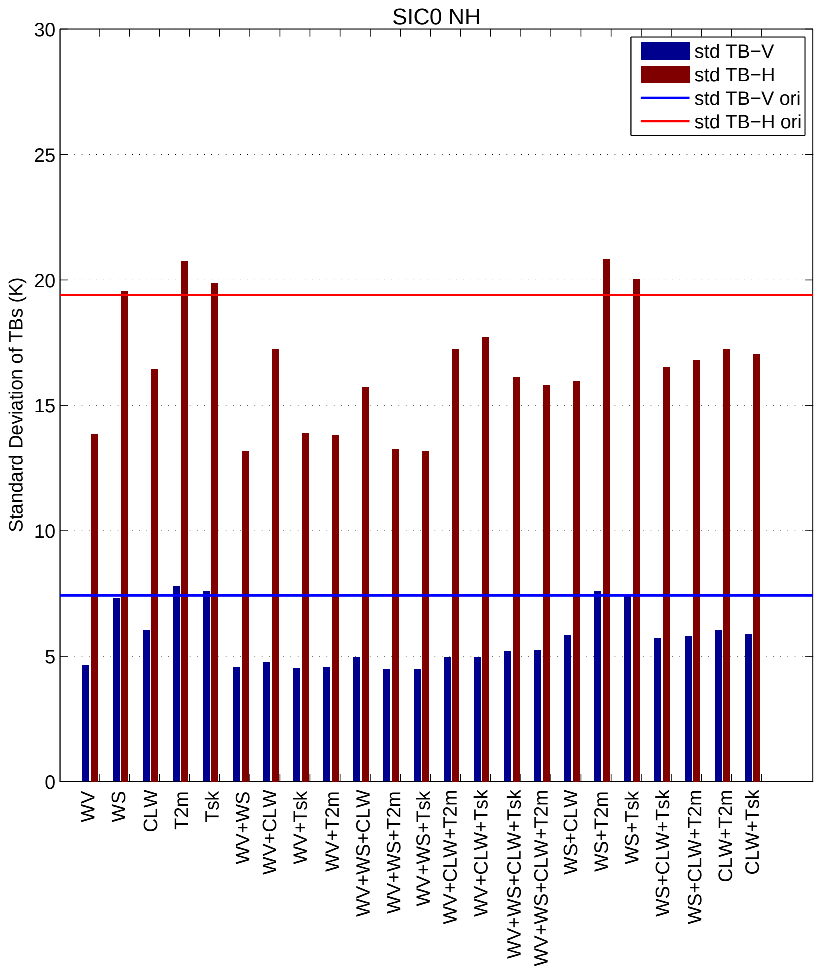

FIGURE 3.8: The standard deviations of brightness temperatures before and after atmospheric corrections in the Arctic over open water. The red and blue lines indicate the standard deviations of horizontally and vertically polarized T_Bs before correction respectively. The red and blue bars show the *std*-T_Bs at horizontal and vertical polarizations after the corrections.

applies little impact. This is probably caused by the temporal discrepancy between the collocated ERA-Interim data and the AMSR-E measurements. Water vapour varies slowly both temporally and spatially, therefore the probability of a good match between the collocated ERA-Interim atmosphere profile and AMSR-E measurement is high. On the contrary, clouds are horizontally more variable than atmospheric water vapour field, thus an effective correction is only possible based on a good temporal match, while the temporal resolution of ERA-Interim is 6h, far too coarse to meet exactly the cloud situation at the times of the AMSR-E measurements.

The effects of the combined corrections are not simply the sum of the involved parameters' effects. For instance, the single skin temperature correction causes a higher *std*-T_B, while after combining with total water vapour, the combined correction has an even better performance than the TWV correction, because higher surface temperatures usually indicate higher total water vapour content (see Figure 3.6). As explained in Chapter 2.2, higher surface temperature alone increases the thermal emission, while TWV is an important component to determine total atmospheric absorption and emission. Hence the combined corrections considering both the surface and the atmosphere are more effective than the single ones. The same argument holds for the correction combining wind speed with water vapour, as the most effective single correction, water vapour is dominant in the combined corrections as well. Those corrections that include water vapour are generally more effective than those without. Among all the 23 applied corrections, the most effective correction is the combination of water vapour, wind speed and T_{skin}, after which the *std*-T_Bs reduces by 27.9% at H-Pol, and by 39.2% at V-Pol.

Figure 3.9 shows the variation of polarization difference before (blue line) and after (blue bars) all possible correction types. The overall trend is almost the similar as in Figure 3.8 except for cloud liquid water correction, which causes a slight increase in *std*-P from 12.9 K to 13.3 K. As discussed in Chapter 3.2.1, cloud liquid water significantly lowers the polarization difference. i.e. P should increase if the LWP is omitted. This could lead to a slightly more scattered distribution of P. In addition to that, this increase is less than 1 K, which is within the statistical error of AMSR-E (approx. 1.2 K). Based on the reduction in standard deviation of the polarization difference, the most effective correction is the combination of TWV, *WS* and T_{skin}, which is also the most effective correction of the single brightness temperatures.

Figure 3.10 illustrates the histograms of the brightness temperatures and the polarization difference before and after the most effective atmospheric correction. The distribution of all three parameters: T_{BH}, T_{BV} and P are much narrower and closer to Gaussian distribution after the correction, especially the vertically polarized brightness temperature.

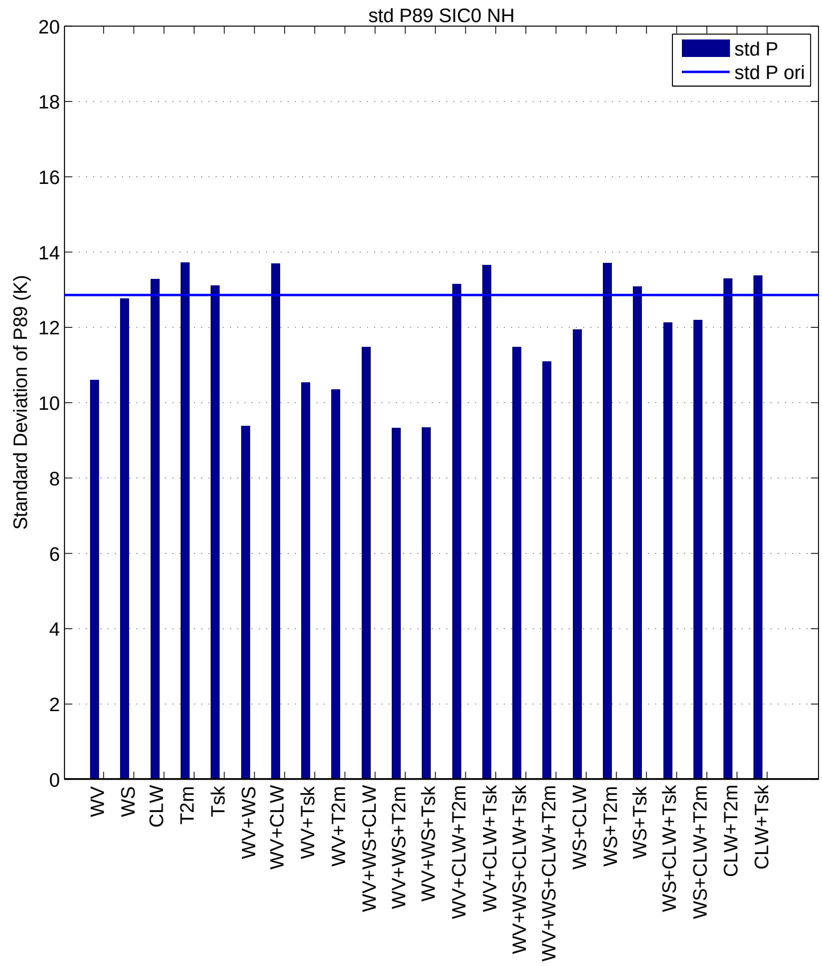

FIGURE 3.9: The standard deviations of polarization difference before and after atmospheric corrections in the Arctic over open water. The blue line indicates the standard deviation of Ps before correction. The blue bars show the *std*-Ps after the corrections.

3.3.2 100% Ice Concentration

All the 23 correction types that are applied to open water are tested on the fully ice covered ocean as well. In addition to that, the effect of the emitting layer temperature, i.e. the temperature at the penetration depth of 89 GHz of snow covered sea ice is also evaluated. The penetration depths of the microwave radiation vary with different ice types and frequencies (Tonboe et al., 2005). Hence the emission measured by the satellite can occur from above and below the penetration depths. Study (Mathew et al., 2009) assumes the emitting layer temperature (T_{emit}) to be the physical temperature of the penetration depths. At lower frequencies, the snow cover on the sea ice is transparent, thus the penetration depth inside the ice

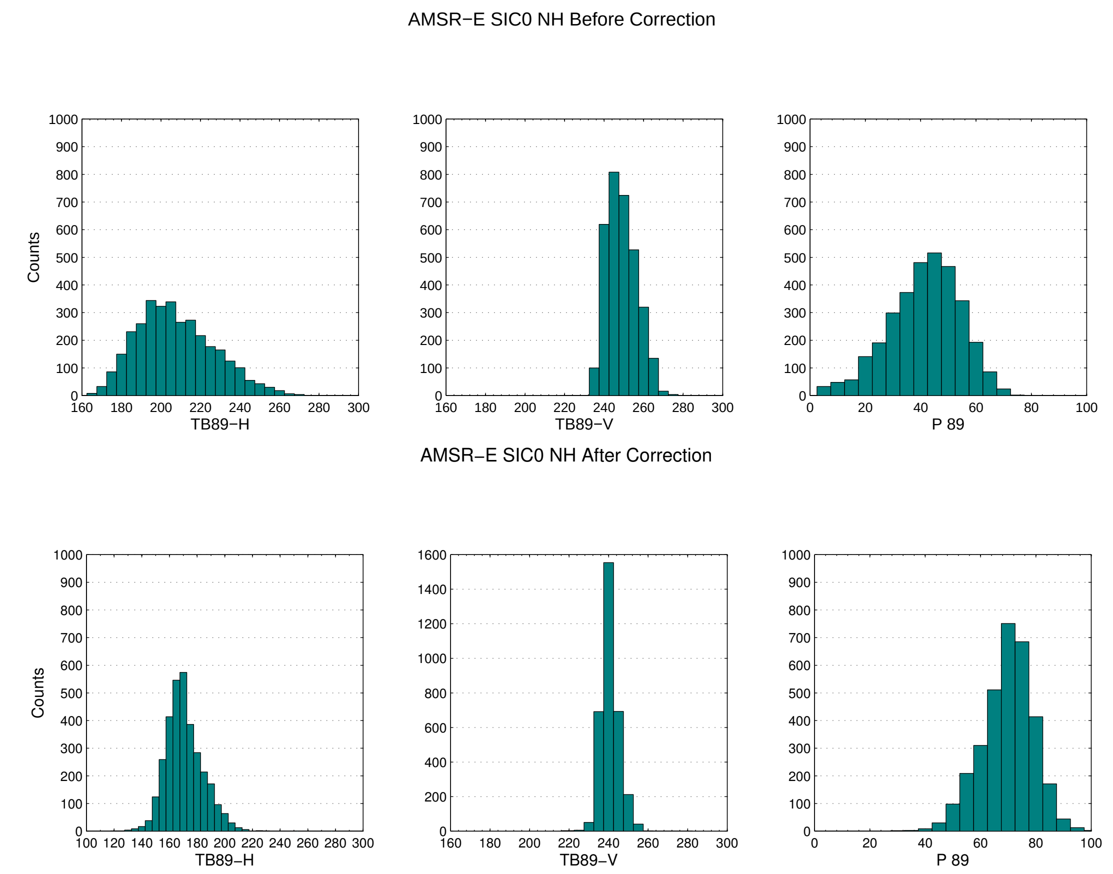

FIGURE 3.10: The histograms of AMSR-E measured brightness temperatures at H- and V- polarizations, and the polarization difference P, before and after correction over open water in the Arctic. The bin size is 5 K for T_{BH} and T_{BV}, and 1 K for P .

is considered. For higher frequencies, the snow cover is larger than the penetration depth, and then the representative emitting layer temperature is inside the snow. Due to the variation of emitting layer depths, the surface temperature products taken from ERA-Interim: 2 meters air temperature and skin temperature, might be different from the emitting layer temperatures of closed ice. Mathew (Mathew et al., 2009) found that T_{emit} is linearly related to the lowest level air temperature (T_{2m}) at AMSR-E frequencies. The retrieval method of the emitting layer temperature is adopted from her study.

The importance of mixed ice surface emissivity to the measured brightness temperatures is discussed in Chapter 3.2.2. In the sensitivity study of simulated brightness

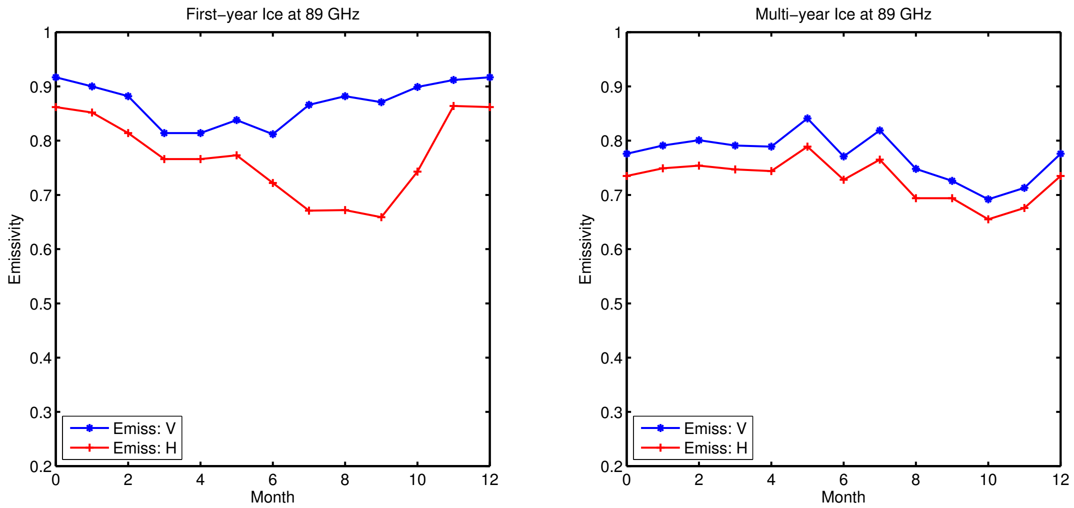

FIGURE 3.11: The monthly averaged emissivities at 89 GHz of First- and Multi-Year ice (Mathew et al., 2009).

temperatures to geophysical parameters, we assume that the emissivities of different ice types are constant over all months. However, the ice emissivities vary a lot during a year due to the variation in its thickness, salinity, the snow cover above, and etc. (Tonboe et al., 2005). For these reasons, constant ice emissivities over all months may not represent the true radiometric characteristics of ice. Therefore we adopt the monthly averaged ice emissivities retrieved in the study (Mathew et al., 2009) to evaluate its influence on the atmospheric correction. Figure 3.11 shows the monthly averaged emissivities of first- and multi-year ice at 89 GHz. Blue asterisks denote V-Pol and red plus symbols denote H-Pol. The lines connecting the data points are only for increasing the plot readability. The seasonal variation of first-year ice emissivities is generally larger than of multi-year ice, especially during the Arctic summer (from June to September) when first-year ice melts into water, and causes the polarization difference in emissivities increase. One disadvantage of using monthly averaged ice emissivities is that an abrupt change might occur between two adjacent months. To smooth out such abrupt variation, we assume the seasonal variation of emissivities is linear, and apply a linear interpolation to calculate the daily emissivity.

The fraction of each ice type is also crucial for the ice surface emissivity due to their different radiometric signatures. The Arctic sea ice can roughly be categorized into new ice, first-year ice and multi-year ice according to its age. In the early stage of ice formation, the brine is not yet completely flushed out, and causes high salinity (usually between 14 and 16‰) in new ice. As the formation carries on, ice gets thicker and has more snow accumulated on the top. This stage is first-year ice. The ice thickness is typically 0.3 to 2 meters, and its emissivity is strongly affected by the micro-structure and water content of its snow cover (Tonboe et al., 2005). As the ice survives the melting seasons, it experiences strong temperature changes reducing its salinity, and turns into multi-year ice. Its snow cover sees melting, recrystallization and form melt ponds. The typical salinity of multi-year ice is below 1‰(Tonboe et al., 2005), and has lower emissivities than first-year ice at higher microwave frequencies (see Figure 1.1). An accurate estimation of ice emission is only possible with a precise ice type retrieval. Here we compute the multi-year ice fraction of the test regions by two different algorithms: NASA Team (Swift et al., 1985) and ECICE algorithm (Shokr et al., 2008).

Figure 3.12 compares the atmospheric correction effects on 100% ice using constant (plots in the upper row) and moving monthly averaged emissivities (plots in the second row). The multi-year ice fraction is retrieved by NASA Team algorithm in the left column, and by ECICE algorithm in the right one. The blue and red lines denote the standard deviation of brightness temperatures before the correction at V-Pol and H-Pol, and the standard deviation of T_{BV} and T_{BH} after each correction are illustrated by the bars. The difference between the plots in each row is small, indicating that by using the same ice emissivities, the correction effects based on the two ice type retrieval algorithms are consistent. Now comparing the plots in each column, the reduction in the standard deviation of T_Bs is more pronounced in the lower row, indicating that the corrections are more effective using moving monthly averaged ice emissivities, and that the monthly varying emissivities more exactly describe the observations than the constant ones. This confirms the generality of contest of first-year and multi-year ice. Note that the used emissivities have been taken at different places and years (Mathew et al., 2009) than the observations used in this study. Henceforth, the corrections are implemented

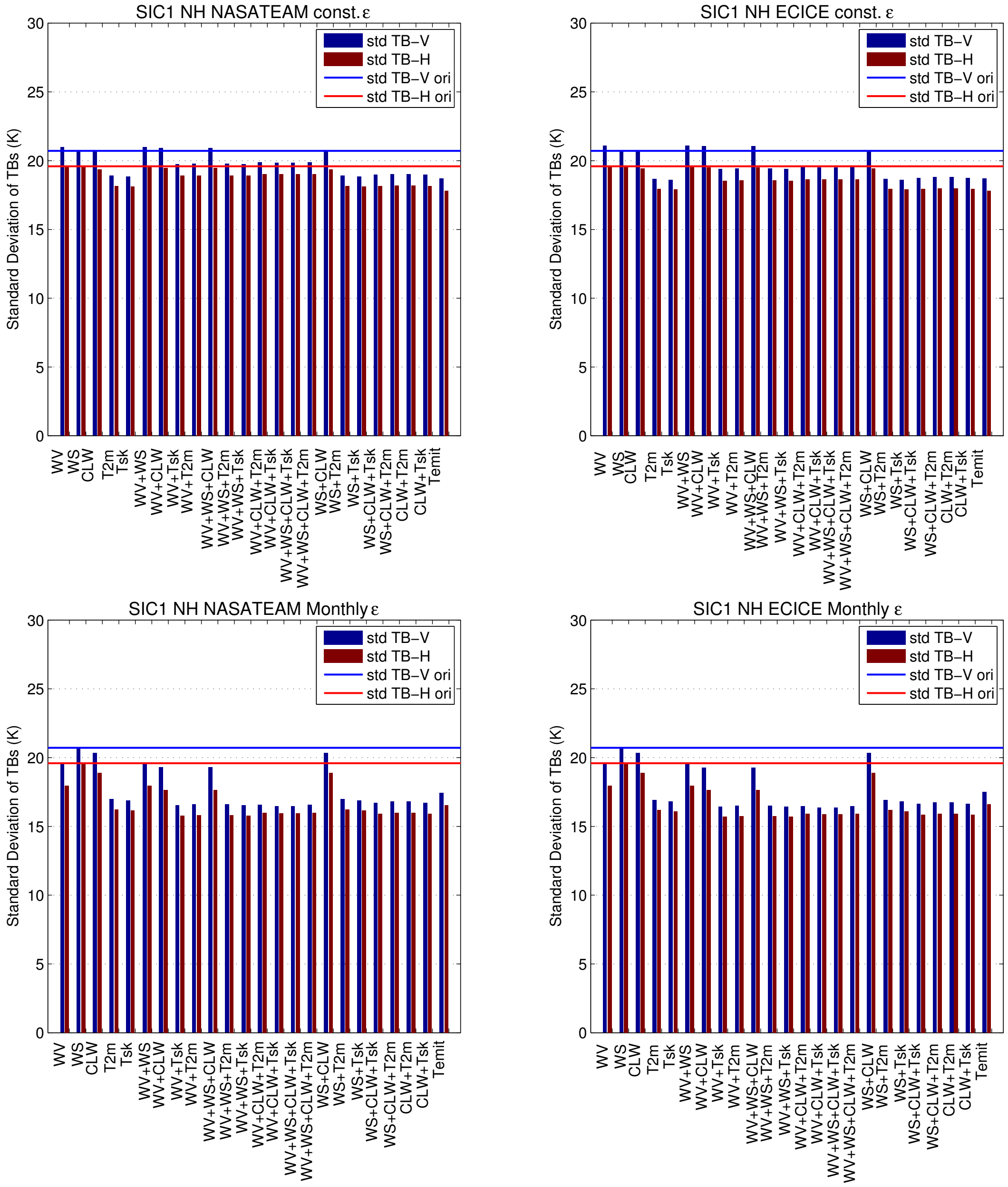

FIGURE 3.12: Comparison of the effects of atmospheric corrections in the Arctic over sea ice based on constant ice emissivities (plots in the first row) and moving monthly averaged ice emissivities (the second row). The red and blue lines indicate the standard deviations of horizontally and vertically polarized T_Bs before correction respectively. The red and blue bars show the *std*-T_Bs at horizontal and vertical polarizations after the corrections. Multi-year ice fraction is calculated by NASA Team algorithm in the left column, and by ECICE algorithm in the right column.

with monthly average ice emissivities, and NASA Team retrieved multi-year ice fraction.

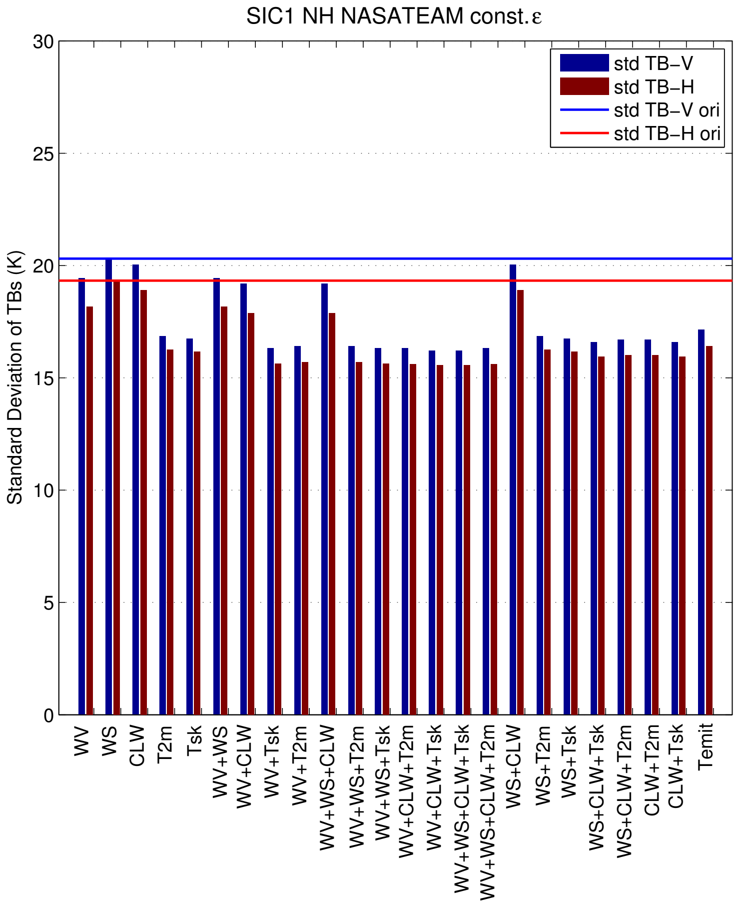

FIGURE 3.13: The standard deviations of brightness temperatures before and after atmospheric corrections in the Arctic over sea ice in winter using moving monthly averaged ice emissivities. The red and blue lines indicate the standard deviations of horizontally and vertically polarized T_Bs before correction respectively. The red and blue bars show the *std*-T_Bs at horizontal and vertical polarizations after the corrections. Multi-year ice fraction is calculated by NASA Team algorithm.

The characteristics of sea ice is more variable during the Arctic summer (Mathew et al., 2009). According to Figure 3.11, the monthly averaged emissivities of first-year ice decreases significantly at horizontal polarization from approx.0.75 in March (the annual sea ice extent maxima) to ca.0.65 in September (the annual sea ice extent minima) (Rigor and Wallace, 2004), close to the horizontal emissivity of open water (see Figure 1.1) due to the melting of ice. Multi-year ice has less seasonal variability, while a sudden variation still occurs during April and August. Hence the retrieved ice emissivities are less valid during summer. The 100% ice validation in RRDP data set is also less reliable (Pedersen and Saldo, 2012). The 100% ice data are validated by the ice drift data and SAR convergence maps in areas of high ice concentration, assuming that the small water fraction is frozen up or closed by ridging after one day's convergence, while in summer the higher surface temperature prevents the freezing, and may cause melt ponds. Therefore the brightness temperatures and polarization difference might have larger variability in summer, and thus influence the evaluation of correction effect which is based on the reduction in standard deviation. To exclude the influence of poor quality validation data, we only apply the corrections on the data from Arctic winter (October to May). In the future work, the effect of atmospheric corrections will also be studied for summer months.

The variations of standard deviation of the brightness temperatures after corrections are displayed in Figure 3.13 . For the six single corrections: water vapour, wind speed, cloud liquid water, lowest level air temperature ,skin temperature and emitting layer temperature, T_{skin} causes the largest reduction in std-T_B, which is interpreted as a sign of effective correction. This is consistent with the result of the sensitivity study of simulated T_Bs to geophysical parameters in Chapter 3.2.2, that ice emitting radiation is more sensitive to surface properties such as temperature and ice types. Using skin temperature as the surface temperature brings a slightly better correction effect than using T_{2m} or T_{emit} though the difference is negligible. The similar performance of corrections in skin temperature and emitting layer temperature proves that the T_{skin} product of ERA-Interim data is highly representative for the emitting temperature of ice. Wind speed has no impact on the ice emission, resulting in the same std-T_Bs after the correction. Correction in water vapour causes a small decrease in the standard deviation by approx. 1 K at both polarizations. Cloud liquid water correction reduces the standard deviation by less than 0.5 K. Both corrections have less effect than over open water, due to the low humidity over ice and the high emissivity of sea ice. As for the combined corrections, for all the corrections that include skin temperature or 2 meters air temperature, their effects are similar to the single correction of the corresponding parameter, with only a small improvement. This again proves that surface properties are more dominant than atmospheric condition for sea ice emission observed from space. The best combined correction is water vapour, cloud liquid water and skin temperature, which reduces the standard deviation by about 4 K at both polarizations. Since the correction in wind speed has no effect on sea ice, and the fact that the effect of correction in water vapour and skin temperature is almost the same as that includes liquid clouds, to allow a consistent correction routine for both open water and ice, we still regard the combination of TWV, WS and T_{skin} as the best correction.

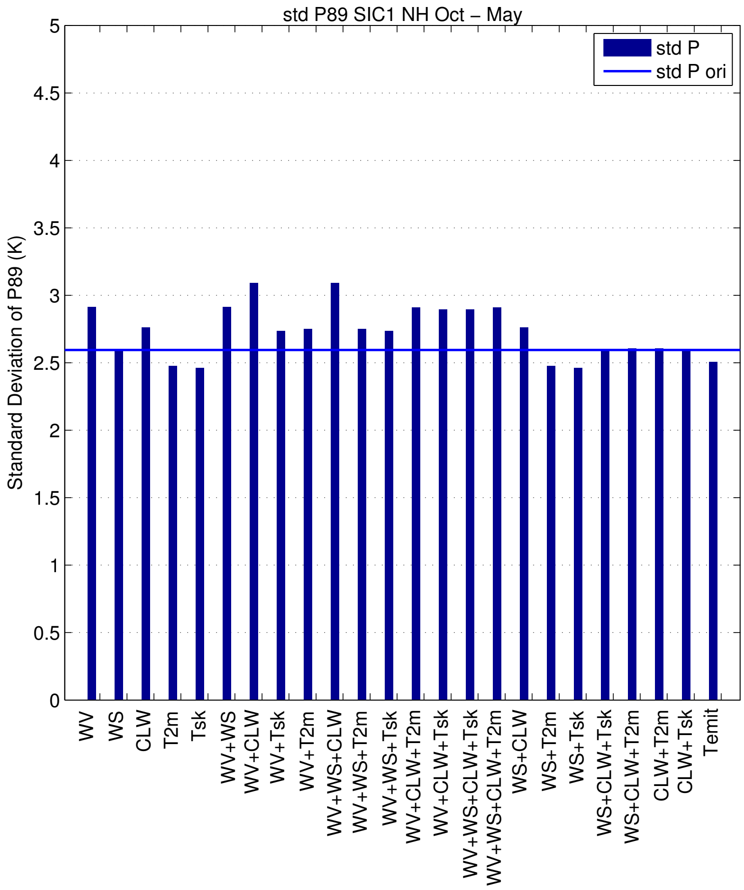

FIGURE 3.14: The standard deviations of polarization difference before and after atmospheric corrections in the Arctic over sea ice in winter using moving monthly averaged ice emissivities. The blue lines indicate the standard deviations of Ps before correction, and the blue bars show the *std-P*s after the corrections. Multi-year ice fraction is calculated by NASA Team algorithm.

Figure 3.14 shows the variation of standard deviation of the polarization differences after all 24 corrections. The overall reduction of the standard deviations in

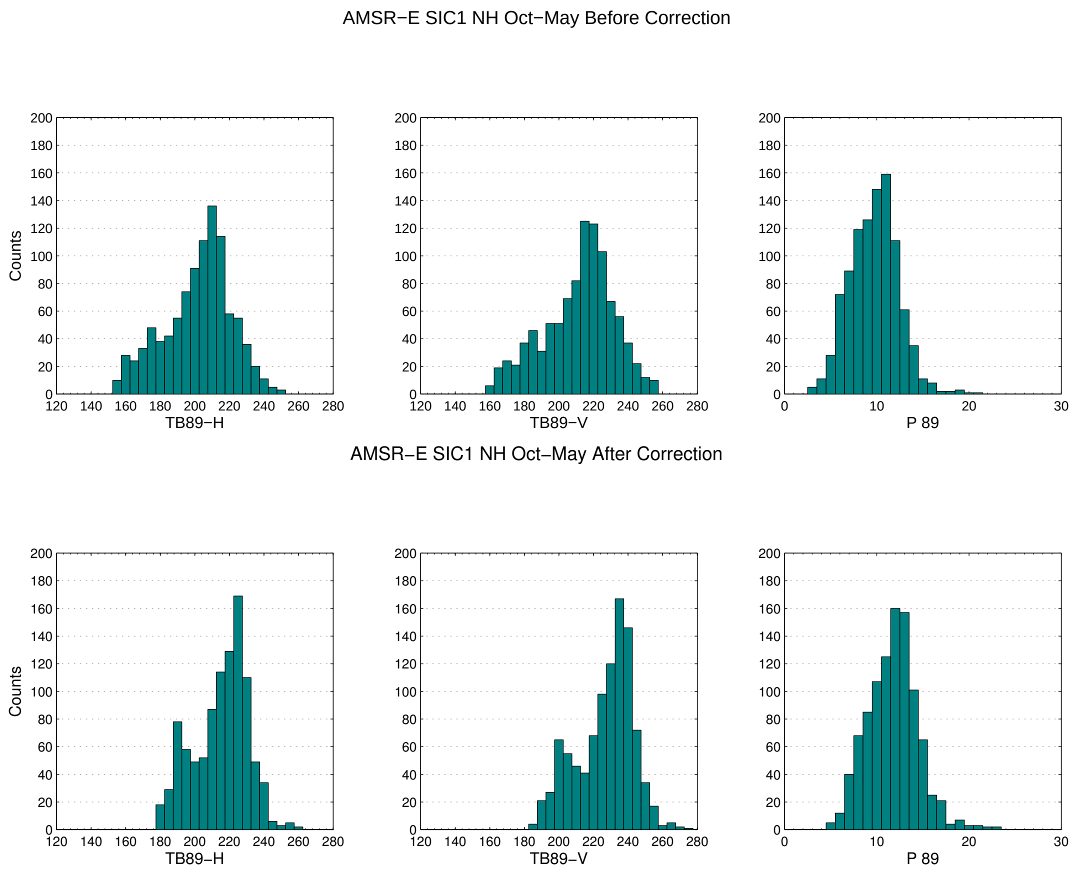

FIGURE 3.15: The histograms of AMSR-E measured brightness temperatures at H- and V- polarizations, and the polarization difference P, before and after correction over sea ice in the Arctic. The bin size is 5 K for T_{BH} and T_{BV}, and 1 K for P .

P is clearly smaller than for the single polarizations (Figure 3.13). In the best case it is about 0.15 K or 6%, whereas for the single polarization it is about 4 K or 20%. The overall trend is the same as that of the brightness temperatures but for total water vapour and cloud liquid water corrections, after which the standard deviations increase by less than 1 K and 0.1 K respectively. The increase in *std*-P in both cases is less than 1 K, might be the sensor noise of AMSR-E. Taken the combined correction of wind speed, total water vapour and skin temperature as the best correction, Figure 3.15 illustrates the distribution of brightness temperatures and polarization difference before and after this correction. For brightness temperatures, the distribution is much narrower, with two visible peaks that indicate the two main ice types: multi-year ice (with the slightly lower T_B due to its lower emissivity) and first-year ice (with the higher T_B). Though according to Figure 3.14 the standard deviation of P slightly increases after the correction, from the histogram such increase is almost negligible.

Chapter 4

Effect of Atmospheric Correction on Retrieved Ice Concentration

According to the reduction in standard deviations of brightness temperatures and polarization difference over open water and over sea ice, the most effective atmospheric correction is selected as the combination of total water vapour, wind speed and skin temperature. In this chapter, ice concentrations are retrieved based on the corrected brightness temperatures, and thus the effect of atmospheric correction on the retrieved ice concentration are assessed. The reduced difference between the retrieved and the reference validated ice concentrations, and the reduction in the standard deviation, are interpreted as good correction effect. Several ice concentration retrieval algorithms are applied, including *ASI_Bootstrap_NWF*, *ASI_NWF* (*NWF* means no weather filter) and *Lin90*.

4.1 New Tie Points

The key parameter to ice concentration retrieval is the tie point, which represents the radiometric characteristics of ice and water under typical conditions of the researched area. Tie points often include the average atmospheric influence as well. As the atmospheric impacts on the brightness temperatures are corrected, the values of tie points must have shifted accordingly. Here we apply a linear transform to calculate the new tie points for the corrected brightness temperatures.

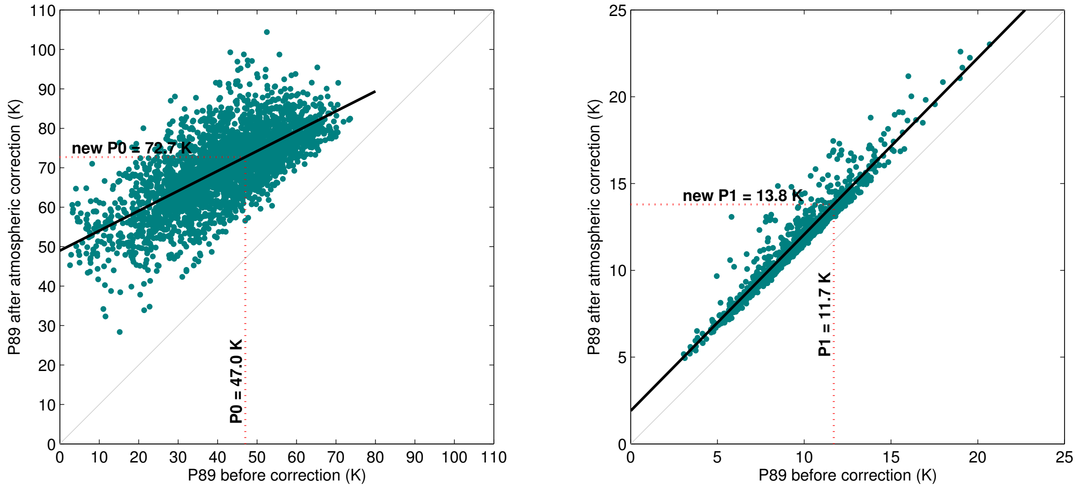

FIGURE 4.1: The scatter plot of polarization difference in brightness temperatures before and after the best atmospheric correction over open water (left) and sea ice (right). The black line shows the linear regression of P, and the two red lines indicate the tie point P_0 and P_1 before and after the correction.

Figure 4.1 shows the scatter plot of the polarization difference in brightness temperatures before and after atmospheric correction over open water (the left plot) and over 100% sea ice (the right plot). The solid black lines are the linear regression for each scatter plot, which represents the linear relationship between the polarization difference before and after correction. Applying this linear transform on the standard tie points of the non-corrected brightness temperatures, the new tie points are calculated as $P_0 = 72.7$ K and $P_1 = 13.8$ K. As shown in the figure, after the combined correction of water vapour, wind speed and skin temperature, the polarization difference over open water has a significantly narrower distribution and higher values, which results in a nearly doubled tie point P_0. Whereas over sea ice, the polarization difference only increases slightly, so does the tie point P_1. This is consistent with the sensitivity study in Chapter 3.2, that geophysical parameters have a higher influence on polarization difference over open water than over sea ice.

4.2 Effect of Atmospheric Correction on Retrieved Ice Concentration

Several ice concentration retrieval algorithms that use the 89 GHz channel are evaluated in this study, including *ASI_Bootstrap_NWF*, *ASI_NWF* and *Lin90*. *ASI_Bootstrap_NWF*, *ASI_BS_NWF* in short, adopts the *Bootstrap* algorithm to screen out open water pixels in additional to the core *ASI* algorithm. All pixels with lower than 5% ice retrieved by *Bootstrap* are considered to be open water. Since the spatial resolution of the frequency channels used by *Bootstrap* is much lower than that of *ASI*, the total ice concentration is first averaged over a large pixel and then interpolated into higher resolution, and thus low ice concentration pixels might be misclassified as open water. To rule out the bias caused by bootstrap filters, *ASI_NWF* is assessed. *ASI_NWF* only includes the *ASI* polynomial, and has no boundary at 0% and 100% concentrations. *Lin90* is a linear retrieval that also uses the polarization difference at 89 GHz, and it adopts the same set of tie points as *ASI_BS_NWF* and *ASI_NWF*.

Figure 4.2 shows the scatter plot of the ice concentration retrieved by the *ASI_NWF* and *Lin90* algorithms and the polarization difference before and after correction over open water and closed ice. Plots in the upper most row are the *ASI* polynomial (blue curve) and *Lin90* lines (red line). In each plot, the standard deviation and the average value of the retrieved ice concentration are printed. Over open water, after the atmospheric correction, the standard deviation of retrieved ice concentration reduces by about 50% for both *ASI_NWF*, and even more for *Lin90*. Due to the lack of boundary condition at 0% and 100%, the ice concentration over open water varies from -20% to 105% before correction. Though the values below zero and above one hundred are not physical, they help to give a realistic standard deviation at the 0% concentration. For the *ASI_NWF* algorithm, the average concentration decreases from 21.04% to 5.89%, whereas for the ideal value of *Lin90*, it reduces from 15.91% to 4.78%, in both cases getting much closer to zero. Although the standard deviation of *C(ASI_NWF)* of open water reduces by a half after the correction, its value is still quite high (above 15%), meaning that many ice concentration values below 15% can't be accurately retrieved. Hence weather filters are still needed. Over sea ice, the standard deviation of *C(ASI_NWF)* increases slightly after correction by 0.22%(SIC) or 9% relatively, while that of *C(Lin90)* reduces by 2.7%(SIC) or 37% relatively. On the other hand, the average ice concentration over ice increases slightly for *ASI_NWF* from 101.20% to 101.76%(SIC), and decreases by about 2% to 103.46%(SIC) for *Lin90*. The increase in standard deviation and mean value of *C(ASI_NWF)* over ice is caused by the different polynomials. Take a closer look at the first row in Figure 4.2. Before the correction, as the polarization difference gets lower than P_1, the ice concentration first increases to about 105% and then decreases to slightly below 100% when P approaches zero. Whereas in the polynomial after correction, the ice concentration increases further when P gets lower than P_1 until P turns zero. Therefore even with the same set of P of values close to P_1, the *ASI* polynomial of corrected brightness temperatures will result in a higher standard deviation and higher mean value of the ice concentration. However, the advantage of using corrected P value is in another point: the ice concentration below, but near 100% will be more correctly retrieved than with the uncorrected P values, where the retrieval tends to return values nearer to 100%.

Figure 4.3 shows the plot of ice concentration retrieved by *ASI_BS_NWF* as a function of polarization difference before and after correction at both SIC 0 and SIC 1. With the boundary condition and *Bootstrap* filter included, the standard deviation of *C(ASI_BS_NWF)* over open water decreases significantly than that of *C(ASI_NWF)* (see Figure 4.2), from 32.89% to 3.85% before correction, and from 15.34% to 1.61% after correction. Note that the atmospheric correction reduces both the standard deviation and the average ice concentration by more than a half. On top of the strong improvement of the SIC 0 retrievals by the atmospheric correction, the *Bootstrap* filtering further improves the results. However, when using the atmospherically corrected data, the *Bootstrap* filter sets the SIC in much smaller number of pixels to zero. In the pixels unaffected by the *Bootstrap* the

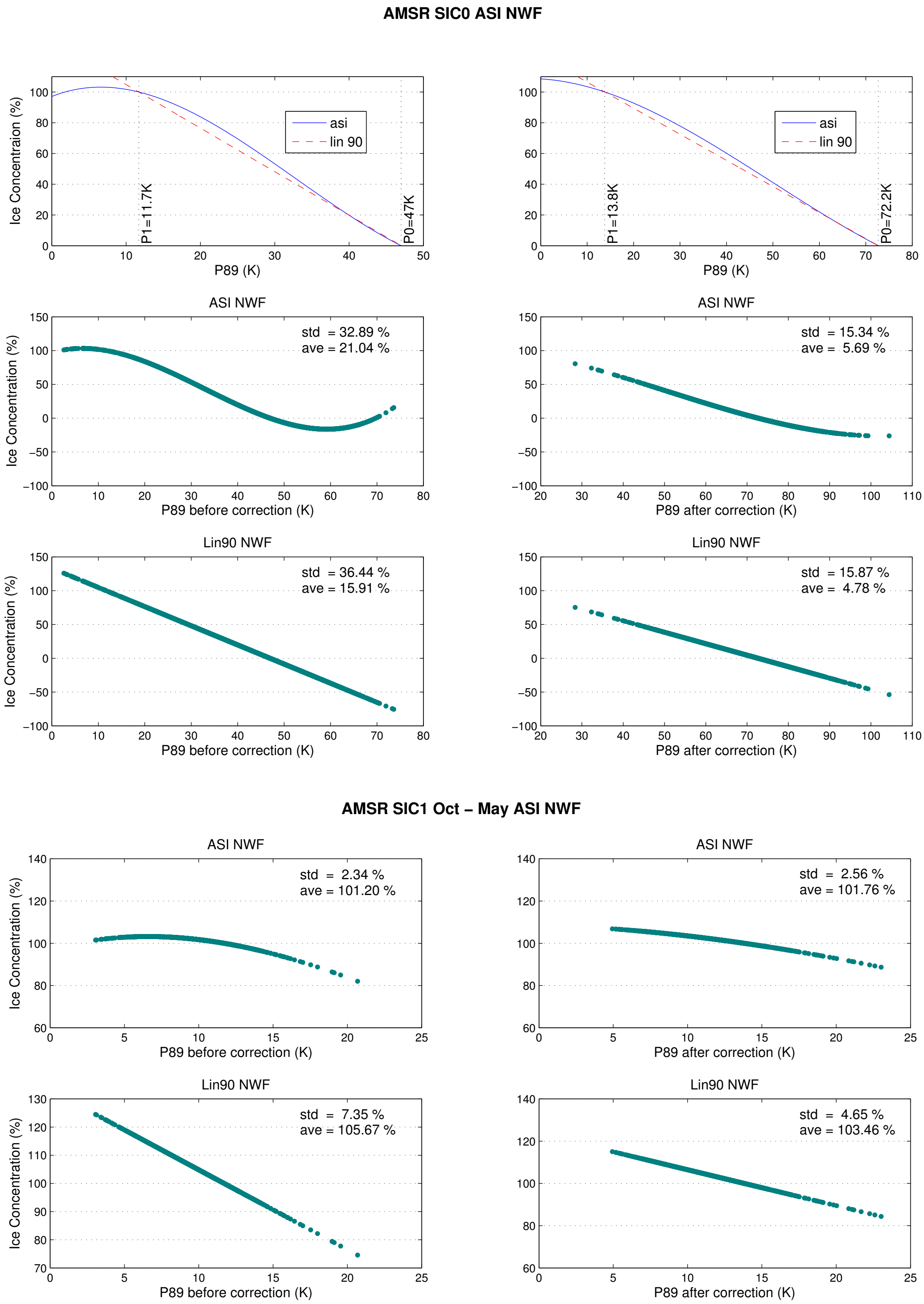

FIGURE 4.2: Ice concentration retrieved by *ASI_NWF* and *Lin90* without cutting off ice beyond 0 and 100%, as function of polarization difference before and after correction. Plots in the upper most row are the *ASI* polynomial (blue curve) and Lin90 line (red line). Ice concentration is retrieved by the *ASI_NWF* and by the *Lin90* algorithm. In each plot, the standard deviation and the average value of the retrieved ice concentration are printed.

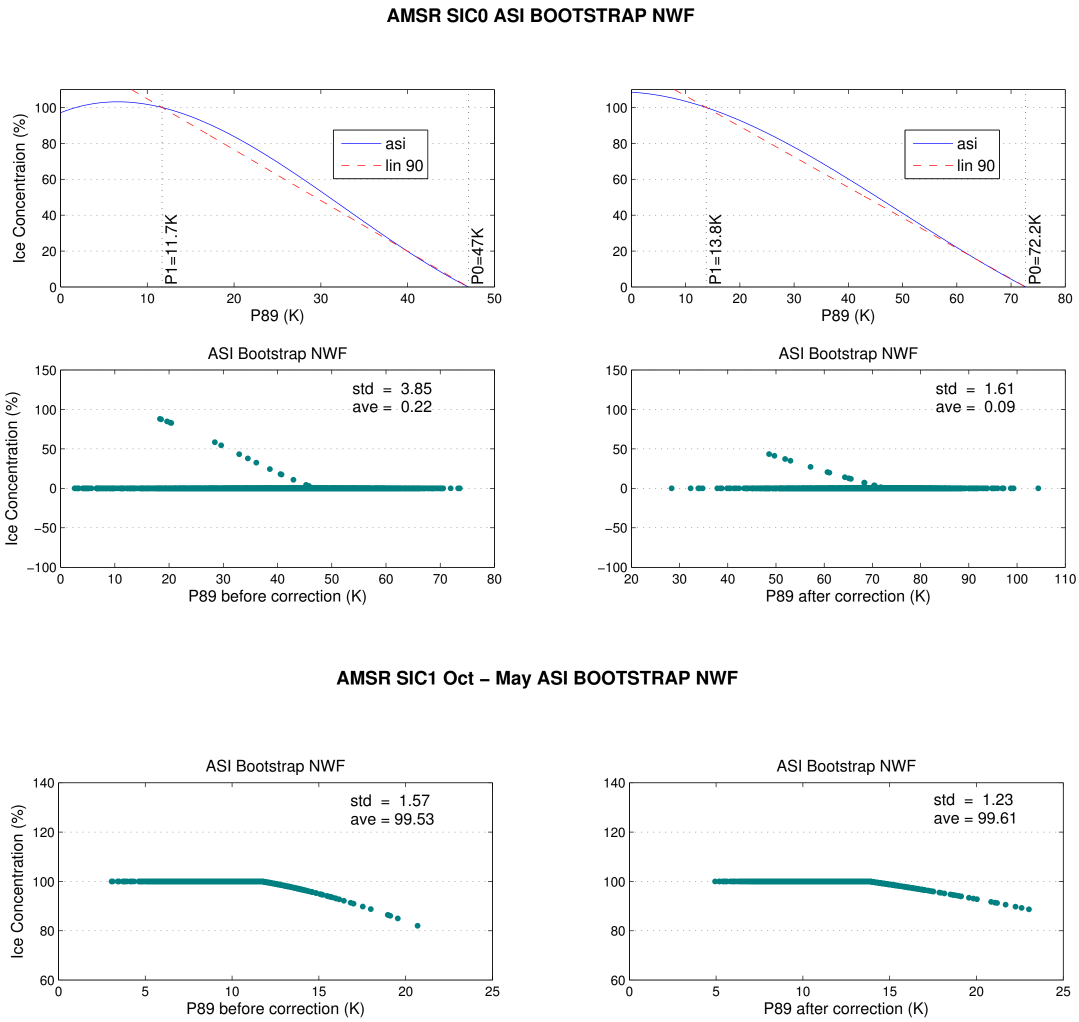

FIGURE 4.3: Ice concentration retrieved by *ASI_NWF* including *Bootstrap* water filtering and correcting ice beyond 0 and 100%, as function of polarization difference before and after correction. Plots in the upper most row show the *ASI* polynomial (blue curve) and Lin90 line (blue line). Ice concentration is retrieved by the *ASI_BS* algorithm. In each plot, the standard deviation and the mean value of the retrieved ice concentration are presented. Over open water, after the atmospheric correction, the standard deviation reduces by more than 50% for *ASI_BS*, and the mean concentration is closer to the reference value 0%. Over sea ice, the standard deviation of *C(ASI_BS)* decreases by 22% after correction.

higher horizontal resolution of the *ASI* ice concentrations is maintained. Moreover, these pixels will show ice concentrations which have been set to zero by the *Bootstrap* filter when using the uncorrected brightness temperatures for *ASI*. In conclusion, the atmospheric correction improves the *ASI* results both in horizontal resolution and in ice concentration values. In order to quantify this improvement, in the future study we will quantify the number of pixels affected by *Bootstrap* filter before and after correction. In addition to that, the *Boostrap* filter will also be included in the *Lin90* algorithm to test its effect.

Over 100% ice concentration, the *Bootstrap* has no effect. The standard deviation and the average value of retrieved ice concentration vary little after correction.

We conclude that over open water, the atmospheric correction has a much larger influence on the retrieved ice concentration than over ice. Regardless of extra filter, the combined correction in TWV, WS and T_{skin} reduces the standard deviation and the average value of the retrieved ice concentration over open water by about a half. With *Bootstrap* filter included, the standard deviation of ice concentration at 0% becomes close to zero. For 100% ice concentration, the influence of the atmospheric correction is negligible. However, applying the atmospheric correction also to brightness temperatures over high ice concentrations allows to apply it to all observations regardless of the ice concentration, largely facilitating the application in real cases. Moreover, the *ASI* polynomial of corrected polarization difference has smaller discrepancy than the polynomial before, meaning that the new algorithm is more sensitive to ice concentrations near 100%. In the application, the non-physical ice concentrations outside the range 0% to 100% should be be set to the boundary values. Henceforth, the *ASI_NWF* algorithm that includes the boundary conditions and uses the corrected brightness temperatures is called *ASI2_NWF*.

4.3 Application Demonstration

By now the atmospheric correction has only been tested on the validation data. In this section we will demonstrate an example of the correction applied on AMSR-E level 2A swath data. One difficulty in the application is to unify the spatial resolution of different frequency channels, and at the mean time to preserve the high resolution of 89 GHz. The ERA-Interim atmospheric parameters have the coarsest resolution (79×79 km^2), while the resolution of *ASI2_NWF* is 6×4 km^2, therefore it is inevitable to interpolate the atmospheric influence to a higher resolution. The correction is carried out as follow. First, the brightness temperatures of the atmospheric influence are simulated at the resolution of 18.7 GHz, which is the coarsest frequency needed for retrieving multi-year ice concentration. Secondly, the simulated brightness temperatures are interpolated into the resolution of 89 GHz, and finally being subtracted from the 89 GHz brightness temperatures. This way the brightness temperatures of high resolution are preserved.

Figure 4.4 visualizes the effect of atmospheric correction on the retrieved ice concentration. The top map shows the *C(ASI_NWF)* and the bottom map displays the *C(ASI2_NWF)*. According to the previous chapters, the best correction is the combination of total water vapour, wind speed and surface temperature. But after applying the correction to swath data, we notice that the combination has an even better effect when cloud liquid water is included. Therefore in the right plot of Figure 4.4, we include *LWP* into the combined correction. The red, green and blue boxes remark the false positive concentrations possibly caused by high water vapour or liquid clouds, because the high values of these two parameters show the similar patterns as the anomalies (see Figure 4.6). Figure 4.5 shows the difference between the ice concentration retrieved by *ASI_NWF* before and after the correction. The ice concentration decreases little by 10% in the centre of the Arctic after the correction, which confirms that the atmospheric correction has little influence at high ice concentrations. Whereas over open ocean, the intensities of false high ice concentrations have significantly reduced by 10% to 70% (SIC) in the red and blue box, and by 10% to 30% (SIC) in the green box. The remaining ice anomalies

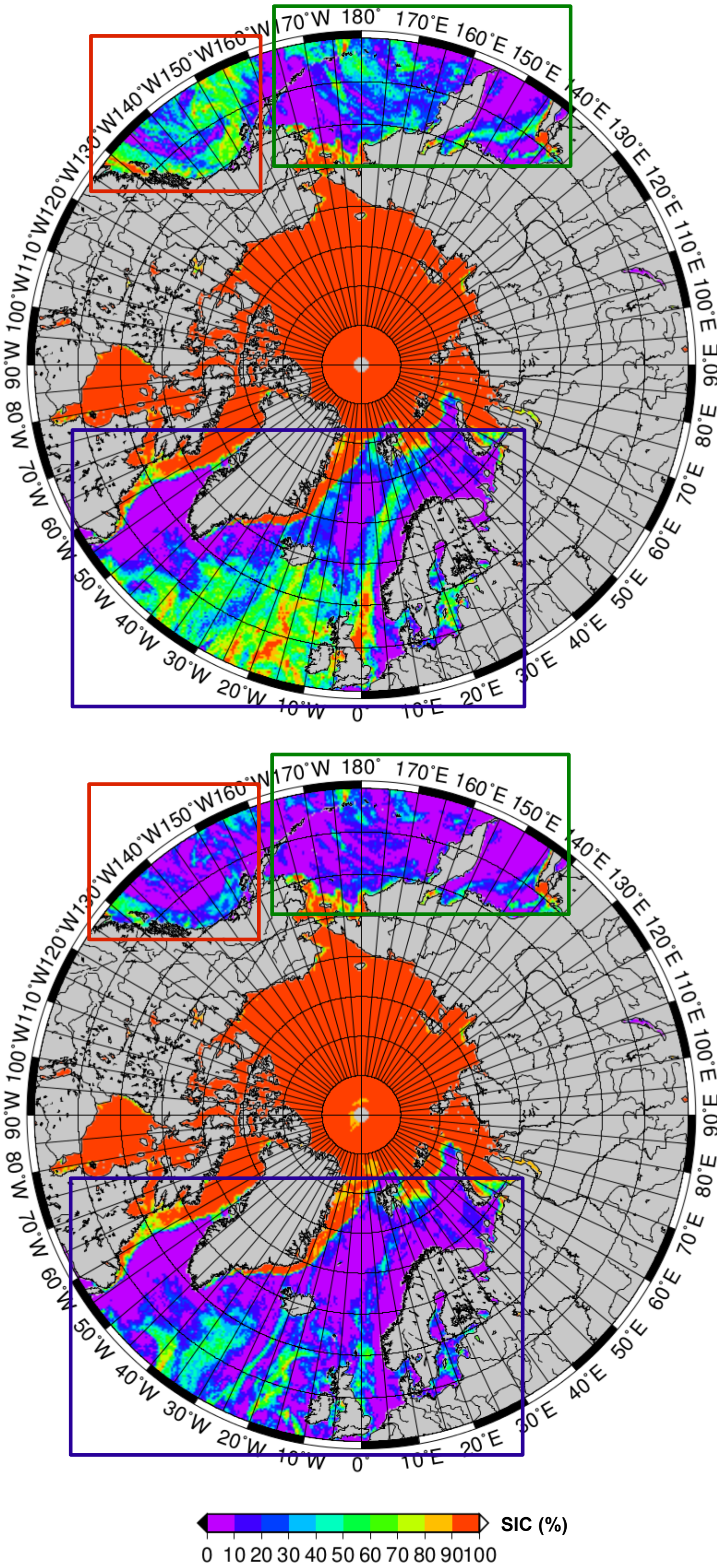

FIGURE 4.4: The ice concentration map retrieved by *ASI_NWF* (top) and by *ASI2_NWF* using corrected brightness temperatures (bottom). The combined correction includes *TWV*, *LWP*, *WS* and T_{2m}. The AMSR-E swath data is from 01. Jan, 2008. The red, green and blue boxes shows the regions of false positive ice concentration caused by high water vapour and liquid clouds.

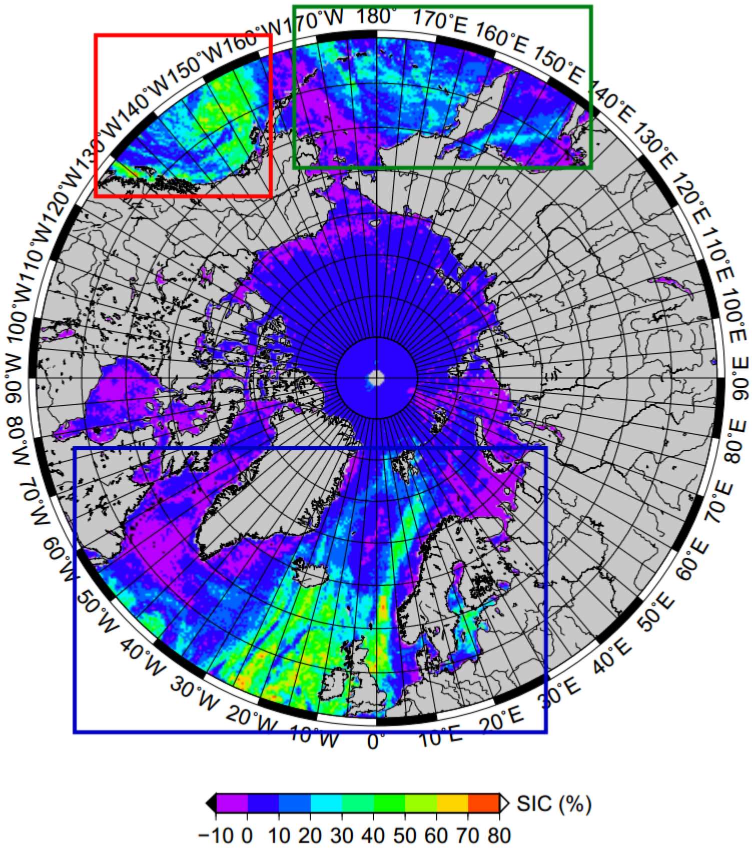

FIGURE 4.5: The difference between ice concentration retrieved by *ASI_NWF* and *ASI2_NWF*

are located at where the high liquid water (according to MODIS image) is not reflected in the ERA-Interim *LWP* data (right plot in Figure 4.6), meaning that the ERA-Interim liquid cloud product does not describe the exact cloud situations of AMSR-E observations. As described in Chapter 3.2.1, the polarization difference at 89 GHz decreases drastically with cloud liquid water over open water. This indicates that a small underestimation of *LWP* will lead to an overestimation of ice concentration, and cause false positive ice concentrations. In order to further improve the atmospheric correction over open ocean, a cloud liquid water product of closer resolution and smaller temporal difference to the 89 GHz observations

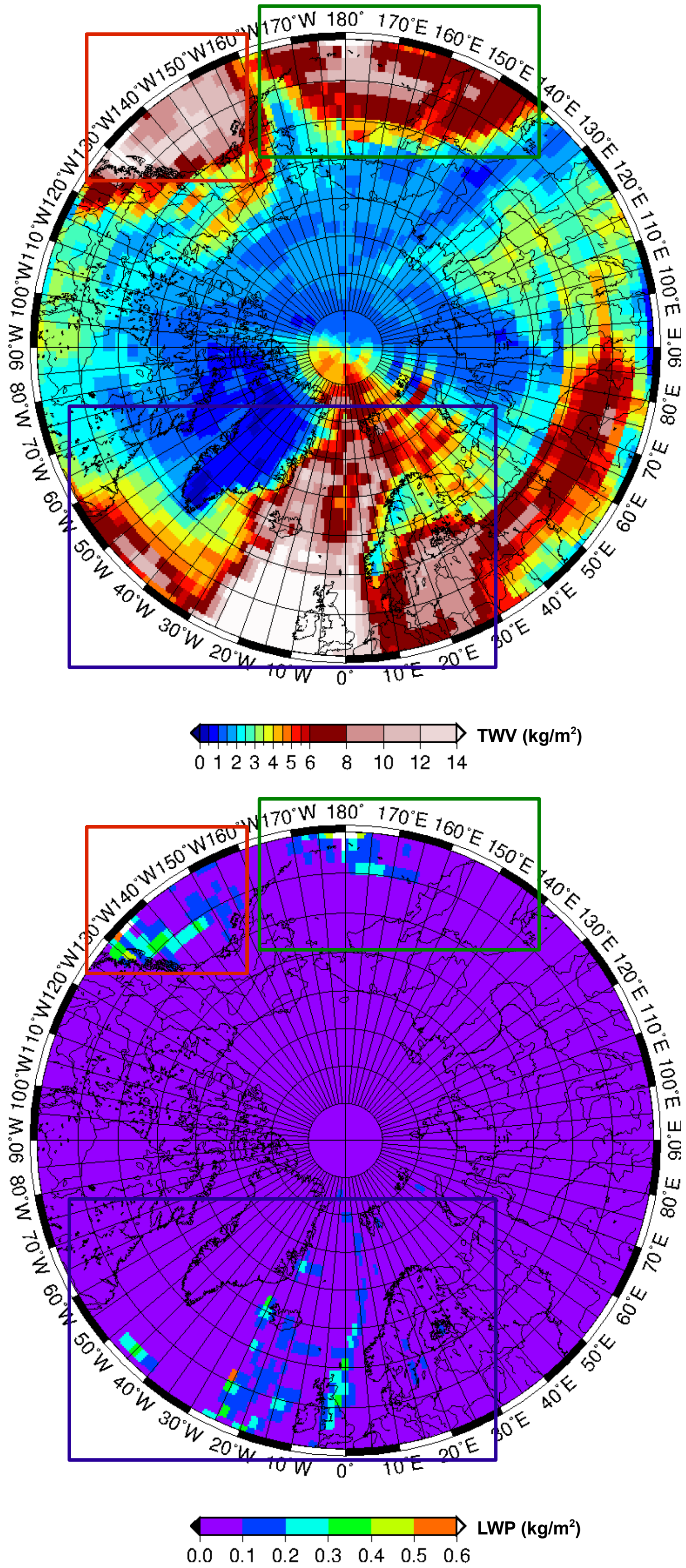

FIGURE 4.6: The co-located ERA-Interim total water vapour (left) and cloud liquid water (right) of the given AMSR-E observations.

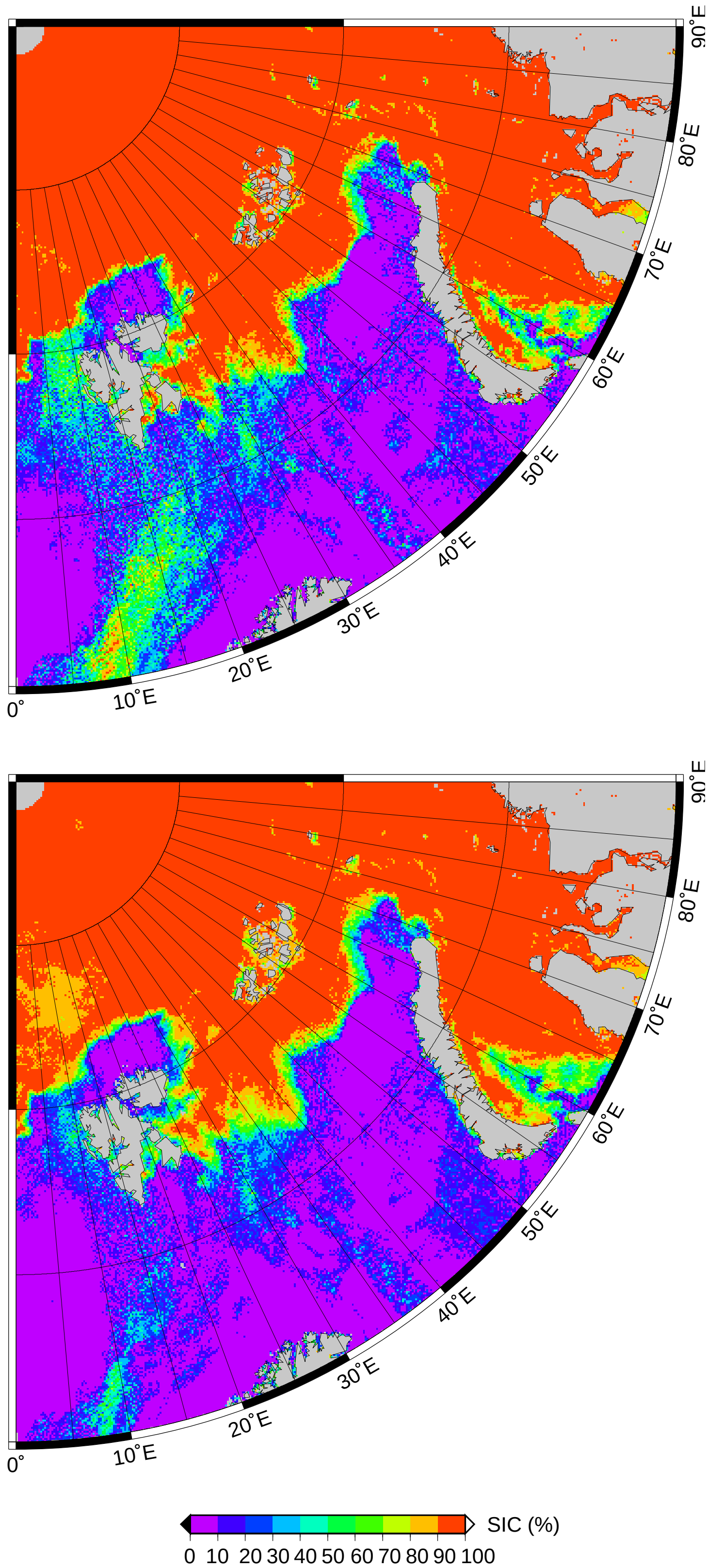

FIGURE 4.7: The effect of atmospheric correction near ice edge. The ice concentration is retrieved by *ASI_NWF* (top) and by *ASI2_NWF* using corrected brightness temperatures (bottom). The combined correction includes *TWV*, *LWP*, *WS* and T_{2m}. The AMSR-E swath data is from 01. Jan, 2008.

would be desirable. Currently in the *PHAROS* group, a new algorithm so called integrated retrieval (Melsheimer et al., 2009), which is also based on the 89 GHz measurements, and retrieves the ice concentration and geophysical parameters at the same time is under development. The atmospheric conditions retrieved by this algorithm are of the same temporal and spatial resolutions with 89 GHz, hence might be used for our future research. While Figure 4.4 shows the reduction of erroneously retrieved ice concentrations over open water at lower latitudes, this effect is much more important near the ice edge. Therefore, Figure 4.7 shows a detailed map of Figure 4.4 in the Barents Sea. The ice edge is slightly broader after the correction. One reason for a broader ice edge is the new *ASI* polynomial, which is closer to linear near 100%. Before the correction, the high ice concentration values tend to be retrieved nearer to 100%, whereas after the correction these values can be more correctly retrieved. The other reason lies in the corrected brightness temperatures. Liquid clouds and water vapour tend to decrease the polarization difference, which is reflected as higher *ASI* ice concentration. When these effects are corrected, the P values will be higher, resulting in slightly lower ice concentrations. Hence near the ice edges, the SIC will decrease less abruptly towards open water. In the future study we will quantify this effect by counting the number of pixels near ice edges with the ice concentration values in the range 80 to 100%.

Chapter 5

Conclusion

The influence of atmospheric parameters on sea ice concentration retrieval in the Arctic is studied, and a new version of the *ASI* algorithm that includes atmospheric correction is developed. The brightness temperatures of open water and closed ice observed from space at 89 GHz react differently to the variation of geophysical parameters. In general, the atmosphere has larger impact on open water than on ice. Four geophysical parameters are tested: total water vapour, liquid water path, wind speed and surface temperature. Under typical Arctic condition, higher TWV (ranging from 0 to 20 kg/m^2) increases the simulated brightness temperatures linearly at both polarizations, and decreases in the polarization difference from approx. 80 K to 50 K over open water (Figure 3.3). Strong wind over open water roughens the surface, resulting to higher overall emissivities (Figure 3.4) and polarization mixing. Therefore the vertically polarized brightness temperatures decrease with increasing wind speed, and the horizontally polarized brightness temperatures increase. Liquid clouds induce non-linear variability of the brightness temperatures and causes less polarization difference. Opposed to our expectation, the simulated T_Bs decrease with increasing surface temperature at both polarizations, because higher sea surface temperatures cause higher dielectric permittivity, resulting to larger reflectance and lower emissivity. Over closed ice (Figure 3.7), the atmospheric properties such as TWV and LWP have less impact than the surface properties (surface temperature and ice types) due to the higher emissivities of first-year than that of multi-year ice. Wind speed has no impact on ice at all. TWV and LWP both decrease the polarization difference of ice as they do over open water, but of a smaller magnitude due to their low concentrations and to the high emissivity of ice. The simulated brightness temperatures increase with higher surface temperature, while the polarization difference remains the same.

All possible atmospheric correction, including single and combined ones, are tested on the 0% sea ice concentration and 100% ice concentration validation data. The reduction in the standard deviation of the brightness temperatures and the polarization difference is interpreted as a sign for good correction. For open ocean, the most effective single correction for both single brightness temperatures and polarization difference is total water vapour, which reduces the standard deviation of T_{BV} by 2.8 K (or 37.8%) and that of T_{BH} by 5.6 K (or 28.9%). The best combined correction is TWV, WS and T_{skin}, which decreases the std-$T_B s$ by 27.9% at H-Pol, and by 39.2% at V-Pol. Since the atmospheric properties are correlated to surface ones, e.g. higher surface temperature usually co-exists with higher water vapour, the correction that combines both properties are more effective than the single ones. Over sea ice, where the surface properties are more dominant, the atmospheric correction has less impact. The effects of corrections are compared by using two sets of ice emissivities (one set is constant, and the other varies with months) and two multi-year ice fraction retrieval algorithms (NASA Team and ECICE). The results of the two algorithms are consistent, while moving monthly ice emissivities (Mathew et al., 2009) brings better correction effects though they were measured in different regions and in a different year. This confirms the reliability of both algorithms, and the generality of the ice emissivities. The most effective single correction over ice is skin temperature, and the best combined correction is TWV, LWP and T_{skin} which reduces the standard deviation by about 4 K (or 20%) for both polarizations. Whereas for the polarization difference, the overall reduction of the standard deviation is smaller than that of single polarizations. In the best case (T_{skin}) it is about 0.15 K. The effect of each single correction is similar to that on single polarizations except for TWV, which increases the standard deviation slightly by 1 K. Such increase can be explained by the effect of combining the uncertainties of two independent variables. In order to provide a consistent correction for both open water and sea ice, we choose the combination of total water vapour, wind speed and skin temperature as the best correction.

The effect of the best correction is then tested on the retrieved ice concentration. A new set of tie points: $P0 = 72.7$ K and $P1 = 13.8$ K are calculated based on the linear regression of the polarization difference before and after correction. The new version of *ASI* algorithm that uses the corrected brightness temperatures and new set of tie points is called *ASI2_NWF*. The combined correction reduces the standard deviation of the retrieved ice concentration over open water by about a half (Figure 4.2). With the *Bootstrap* filter included in the retrieval, the standard deviation of ice concentration at SIC 0 becomes close to zero (Figure 4.3). For 100% ice concentration, the influence of atmospheric correction is limited. But the *ASI* polynomial of corrected polarization difference has smaller discrepancy than the polynomial before, meaning that the new algorithm is more sensitive to ice concentrations close to 100%. A linear algorithm (*Lin90*) using the same set of tie points as *ASI* is evaluated as well. The atmospheric correction has similar effect on *Lin90* (Figure 4.2) as on *ASI_NWF* over both open water and closed ice. However the influence of *Bootstrap* filter has not been tested on *Lin90*, and will be part of the future study.

Finally, the combined correction is applied on AMSR-E level 2A spatially resampled data. Though the best correction on the validation data does not include cloud liquid water, after applying the correction to swath data, more ice anomalies over open water are filtered out when LWP is included. The atmospheric correction effectively reduces the false high ice concentrations at lower latitude regions over open water by about 50% to 60%. But due to the much coarser temporal resolution of ERA-Interim products, the LWP data does not describe the exact liquid cloud situation of AMSR-E observations, resulting to the remaining false positive. To further improve the atmospheric correction, a LWP product with closer temporal and horizontal resolution to 89 GHz is needed. Near the ice edge

(Figure 4.7), the correction results in a slightly broader edge area, due to the more linear *ASI* polynomial, and the corrected brightness temperatures. After the correction, the resulting polarization differences of regions with high liquid water and/or water vapour are higher. To further study the effect of correction near ice edges, the pixels with ice concentrations values inside the range 80% to 100% will be quantified in the future study.

Bibliography

AMSR-E instrument description. http://nsidc.org/data/docs/daac/amsre_instrument.gd.html, 2014.

A. Beitsch, L. Kaleschke, and S. Kern. Investigating high-resolution AMSR2 sea ice concentrations during the february 2013 fracture event in the beaufort sea. *Remote Sensing*, 6(5):3841–3856, 2014. ISSN 2072-4292. doi: 10.3390/rs6053841. URL http://www.mdpi.com/2072-4292/6/5/3841.

P. Berrisford, D. Dee, P. Poli, R. Brugge, K. Fielding, M. Fuentes, P. Kallberg, S. Kobayashi, S. Uppala, and A. Simmons. The ERA-Interim archive version 2.0. Technical Report 1, ECMWF, November 2011.

J. Comiso, D. Cavalieri, and T. Markus. Sea ice concentration, ice temperature, and snow depth using AMSR-E data. *Geoscience and Remote Sensing, IEEE Transactions on*, 41(2):243–252, Feb 2003. ISSN 0196-2892. doi: 10.1109/TGRS.2002.808317.

J. C. Comiso, T. C. Grenfell, D. L. Bell, M. A. Lange, and S. F. Ackley. Passive microwave in situ observations of winter weddell sea. *Journal of Geophysical Research: Oceans (1978 - 2012)*, 94(C1), 1989. ISSN 10891-10905.

D. P. Dee, S. M. Uppala, A. J. Simmons, P. Berrisford, P. Poli, S. Kobayashi, U. Andrae, M. A. Balmaseda, G. Balsamo, P. Bauer, P. Bechtold, A. C. M. Beljaars, L. van de Berg, J. Bidlot, N. Bormann, C. Delsol, R. Dragani, M. Fuentes, A. J. Geer, L. Haimberger, S. B. Healy, H. Hersbach, E. V. Hólm, L. Isaksen, P. Kållberg, M. Köhler, M. Matricardi, A. P. McNally, B. M. Monge-Sanz, J.-J. Morcrette, B.-K. Park, C. Peubey, P. de Rosnay, C. Tavolato, J.-N. Thépaut, and F. Vitart. The ERA-Interim reanalysis: configuration and performance of the data assimilation system. *Quarterly Journal of the Royal Meteorological Society*, 137(656):553–597, 2011. ISSN 1477-870X. doi: 10.1002/qj.828. URL http://dx.doi.org/10.1002/qj.828.

ECMWF. Reanalysis at ECMWF. http://old.ecmwf.int/research/era/do/get/Reanalysis_ECMWF, 2008.

R. Fuhrhop, T. C. Grenfell, G. Heygster, K.-P. Johnsen, P. Schlüssel, M. Schrader, and C. Simmer. A combined radiative transfer model for sea ice, open ocean, and atmosphere. *Radio Science*, 33(2):303–316, 1998.

G. Heygster, M. Huntemann, N. Ivanova, R. Saldo, and L. Toudal. Response of passive microwave sea ice concentration algorithms to thin ice. *Proc. IGARSS*, 2014.

W. Ho and W. Hall. Measurements of the dielectric properties of seawater and NaCl solutions at 2.65 GHz. *Journal of Geophysical Research*, 78(27):6301–6315, 1973.

K. Imaoka, T. Sezai, T. Takeshima, T. Kawanishi, and A. Shibata. *Instrument characteristics and calibration of AMSR and AMSR-E*, volume 1, pages 18–20. 2002. doi: 10.1109/IGARSS.2002.1024927.

L. Kaleschke, G. Heygster, C. Lüpkes, A. Bochert, J. Hartmann, J. Haarpaintner, and T. Vihma. SSM/I sea ice remote sensing for mesoscale ocean-atmosphere interaction analysis: Ice and icebergs. *Canadian Journal of Remote Sensing*, 27 (5):526–537, 2001.

L. Klein and C. T. Swift. An improved model for the dielectric constant of sea water at microwave frequencies. *Antennas and Propagation, IEEE Transactions on*, 25(1):104–111, 1977.

N. Mathew, G. Heygster, and C. Melsheimer. Surface emissivity of the Arctic sea ice at AMSR-E frequencies. *Geoscience and Remote Sensing, IEEE Transactions on*, 47(12):4115–4124, Dec 2009. ISSN 0196-2892. doi: 10.1109/TGRS.2009.2023667.

C. Melsheimer, G. Heygster, N. Mathew, and L. T. Pedersen. Retrieval of sea ice emissivity and integrated retrieval of surface and atmospheric parameters over the Arctic from AMSR-E data. *Journal of the Remote Sensing Society of Japan (Japan)*, 2009.

L. T. Pedersen and R. Saldo. *Sea Ice Concentration (SIC) Round Robin Data Package*, November 2012.

I. G. Rigor and J. M. Wallace. Variations in the age of Arctic sea-ice and summer sea-ice extent. *Geophysical Research Letters*, 31(9):n/a–n/a, 2004. ISSN 1944-8007. doi: 10.1029/2004GL019492. URL http://dx.doi.org/10.1029/2004GL019492.

J. Saxton. Dielectric dispersion in pure polar liquids at very high radio-frequencies. ii. relation of experimental results to theory. *Proceedings of the Royal Society of London. Series A. Mathematical and Physical Sciences*, 213(1115):473–492, 1952.

M. Shokr, A. Lambe, and T. Agnew. A new algorithm (ecice) to estimate ice concentration from remote sensing observations: An application to 85 GHz passive microwave data. *Geoscience and Remote Sensing, IEEE Transactions on*, 46 (12):4104–4121, Dec 2008. ISSN 0196-2892. doi: 10.1109/TGRS.2008.2000624.

G. Spreen, L. Kaleschke, and G. Heygster. Sea ice remote sensing using AMSR-E 89-GHz channels. *Journal of Geophysical Research: Oceans*, 113(C2), 2008. ISSN 2156-2202. doi: 10.1029/2005JC003384. URL http://dx.doi.org/10.1029/2005JC003384.

E. Svendsen, C. Matzler, and T. C. Grenfell. A model for retrieving total sea ice concentration from a spaceborne dual-polarized passive microwave instrument operating near 90 GHz. *International Journal of Remote Sensing*, 8(10):1479–1487, 1987. doi: 10.1080/01431168708954790. URL http://dx.doi.org/10.1080/01431168708954790.

C. T. Swift, L. S. Fedor, and R. O. Ramseier. An algorithm to measure sea ice concentration with microwave radiometers. *Journal of Geophysical Research: Oceans*, 90(C1):1087–1099, 1985. ISSN 2156-2202. doi: 10.1029/JC090iC01p01087. URL http://dx.doi.org/10.1029/JC090iC01p01087.

R. Tonboe, S. Andersen, L. Toudal, and G. Heygster. Sea ice emission modelling applications. *Radiative transfer models for microwave radiometry*, 2005.

F. J. Wentz and T. Meissner. Algorithm theoretical basis document version 2 AMSR ocean algorithm, 2000.